

## New hot subdwarf stars identified in Gaia DR2 with LAMOST DR5 spectra - II.

ZHENXIN LEI,<sup>1,2</sup> JINGKUN ZHAO,<sup>1</sup> PÉTER NÉMETH,<sup>3,4</sup> AND GANG ZHAO<sup>1</sup>

<sup>1</sup>*Key Laboratory of Optical Astronomy, National Astronomical Observatories, Chinese Academy of Sciences, Beijing 100012, China*

<sup>2</sup>*College of Science, Shaoyang University, Shaoyang 422000, China*

<sup>3</sup>*Astronomical Institute of the Czech Academy of Sciences, CZ-251 65, Ondřejov, Czech Republic*

<sup>4</sup>*Astroserver.org, 8533 Malomsok, Hungary*

(Received ; Revised; Accepted)

Submitted to

### ABSTRACT

388 hot subdwarf stars have been identified by using the Hertzsprung-Russell (HR) diagram built from the second data release (DR2) of the Gaia mission. By analyzing their observed LAMOST spectra, we characterized 186 sdB, 73 He-sdOB, 65 sdOB, 45 sdO, 12 He-sdO and 7 He-sdB stars. The atmospheric parameters of these stars (e.g.,  $T_{\text{eff}}$ ,  $\log g$ ,  $\log(n\text{He}/n\text{H})$ ) are obtained by fitting the hydrogen (H) and helium (He) line profiles with synthetic spectra calculated from non-Local Thermodynamic Equilibrium (non-LTE) model atmospheres. Among these stars, we have 135 new identified hot subdwarfs which have not been cataloged before. Although 253 stars appear in the catalog by Geier et al. (2017), but only 91 of them have atmospheric parameters. Together with the 294 hot subdwarf stars found by Lei et al. (2018), we identified 682 hot subdwarf stars in total by using the Gaia HR-diagram and LAMOST spectra. These results demonstrate the efficiency of our method to combine large surveys to search for hot subdwarf stars. We found a distinct gap in our He-sdOB stars based on their He abundance, which is also presented in extreme horizontal branch (EHB) stars of the globular cluster (GC)  $\omega$  Cen. The number fraction of the sample size for the two sub-groups is very different between the two counterparts. However, the distinct gap between the H-sdB stars and He-sdOB stars in  $\omega$  Cen is not visible in our sample. More interestingly, the He-sdB population with the highest He abundance in our sample is completely missing in  $\omega$  Cen. The discrepancy between our field hot subdwarf stars and the EHB stars in  $\omega$  Cen indicate different origins for the two counterparts.

*Keywords:* (stars:) Hertzsprung-Russell and CM diagrams, (stars:) subdwarfs, surveys

### 1. INTRODUCTION

Hot subdwarf (e.g., spectral type sdB, sdO and other sub-types of) stars are the exposed helium burning cores of red giant branch (RGB) stars. They have low stellar masses around  $0.5 M_{\odot}$  and very thin H-rich envelopes (e.g.,  $\leq 0.01 M_{\odot}$ ; Heber 2009). Hot subdwarf stars play very important roles in many aspects of astrophysics. Studies on the formation of these special blue stars will vastly improve our understanding on stellar structure and evolution of low mass stars (Han et al. 2002, 2003). Pulsating hot subdwarfs studied by asteroseismology give insights into their interior structures (Kawaler et al. 2010; Charpinet et al. 2011; Baran et al. 2012; Battich et al. 2018; Zong et al. 2018). Furthermore, the variety of surface chemical compositions in hot subdwarfs stars make them good samples to study atmotic diffusion processes (Hu et al. 2009, 2010, 2011; Naslim et al. 2013; Moehler et al. 2014; Jeffery et al. 2017; Németh 2017; Byrne et al. 2018). Study on the counterparts of field hot subdwarfs in GCs (e.g., EHB stars)

Corresponding author: Gang Zhao  
 gzha@nao.cas.cn

Corresponding author: Zhenxin Lei  
 zxlei@nao.cas.cn

can help us understand the formation history and evolution processes of these old populations (Lei et al. 2015, 2016; Latour et al. 2014, 2018). For a recent review on hot subdwarf stars see Heber (2009, 2016).

Binary evolution is considered as the main formation channel of hot subdwarf stars, since about half of these stars are found in close binaries (Maxted et al. 2001; Napiwotzki et al. 2004; Copperwheat et al. 2011). On the theoretical side, Han et al. (2002, 2003) conducted detailed binary evolution and found that Roche lobe overflow (RLOF), common envelope (CE) ejection and merger of two He white dwarfs (WDs) can form sdB stars in binary systems with their properties matching well with the observations. Recently, Kawka et al. (2015) have reviewed the properties of hot subdwarf binary population and measured the orbital parameters of seven close binaries comprising hot subdwarf stars selected from the Galaxy Evolution Explorer (*GALEX*, Morrissey et al. 2007) survey, while in a similar study Kupfer et al. (2015) presented the orbital and atmospheric parameters and put constraints on the nature of the companions of 12 close sdB stars found in the project Massive Unseen Companions to Hot Faint Underluminous Stars from SDSS (MUCHFUSS). Zhang & Jeffery (2012) found that the merger of two He-WDs can reproduce the observed distribution of He-rich hot subdwarf stars in terms of effective temperatures, surface gravities, nitrogen and carbon abundances. Moreover, Zhang et al. (2017) found that the mergers of He-WDs with low mass main-sequence (MS) stars can form intermediate He-rich hot subdwarf stars. Recent progress in this field can be found in Chen et al. (2013), Xiong et al. 2017, Wu et al. 2018 and Vos et al. 2019.

Hot subdwarf stars consist of several sub-types according to their spectral features, such as sdB, sdO, sdOB, He-sdB, He-sdO and He-sdOB (Moehler et al. 1990; Geier et al. 2017a). Moehler et al. (1990) introduced a detailed spectral classification scheme for hot subdwarf stars, which is also widely used today. In this scheme, the spectral features of hot subdwarfs with different sub-types were described with details, including their differences to B type main-sequence stars, blue horizontal branch (BHB) stars and white dwarfs (WDs). Recently, Drilling et al. (2013) defined a more sophisticated MK-like classification scheme for hot subdwarf stars. They found that a spectral class, a luminosity class and a helium class is necessary to classify these hot stars. Moreover, they also give a preliminary calibration between the new spectral classification and atmospheric parameters (e.g., effective temperature, surface gravity, and surface helium-to-hydrogen abundance ratio).

Spectral analysis is the ordinary method to obtain atmospheric parameters (e.g., effective temperature, gravity) and surface chemical abundances of hot subdwarf stars. Lisker et al. (2005) analyzed sdB stars found in the ESO Supernova Ia Progenitor Survey (ESO-SPY, Napiwotzki et al. 2001) by using metal line-blanketed LTE models of solar composition and the LINFOR program for spectrum synthesis (Heber et al. 1999, 2000). On the other hand, Stroeer et al. (2007) analyzed O type subluminous stars of the same sample by using non-LTE models with H/He composition. These models were calculated with the TMAP package (Werner & Dreizler 1999; Rauch & Deetjen 2003; Werner et al. 2003). Vennes et al. (2011) computed a grid of non-LTE model atmospheres and synthetic spectra by using the codes TLUSTY-SYNSPEC (Hubeny & Lanz 1995; Lanz & Hubeny 1995) to analyze hot subdwarf stars in the *GALEX* survey (Morrissey et al. 2007). Moreover, Németh et al. (2012) obtained the atmospheric parameters of 166 sdB/O stars found in the *GALEX* survey by using H/He/CNO non-LTE model atmospheres with H/He/CNO composition calculated with TLUSTY-SYNSPEC. For recent progress in this field see Moni Bidin et al. (2012); Latour et al. (2013, 2015, 2016), etc.

Due to the significance of hot subdwarfs in astrophysics, many new hot subdwarf stars were discovered in large spectral surveys, such as Kepler (Østensen et al. 2010), *GALEX* (Vennes et al. 2011; Németh et al. 2012; Kawka et al. 2015), the Sloan Digital Sky Survey (SDSS, Geier et al. 2015; Kepler et al. 2015, 2016) and the Large Sky Area Multi-Object Fibre Spectroscopic Telescope (LAMOST) survey (Luo et al. 2016). Geier et al. (2017a) compiled a large hot subdwarf catalog which contains 5613 objects by retrieving known hot subdwarfs and candidates from the literature and unpublished databases. In this catalog, many useful information of the stars are listed, such as multi-band photometry, proper motions, classifications, atmospheric parameters, etc. Furthermore, Geier et al. (2019) compiled an all-sky catalog of 39 800 hot subluminous star candidates, which were selected from the Gaia DR2 database (Gaia Collaboration et al. 2018a) by means of colour, absolute magnitude and reduced proper motion cuts. The majority of the candidates in this catalog are expected to be hot subdwarf stars, and it can be used as an input catalog for future photometric and spectroscopic surveys.

With the DR2 of the Gaia mission (Gaia Collaboration et al. 2018a), we expect a large number of new hot subdwarf stars to be uncovered. Gaia DR2 provide accurate astrometry (e.g., parallaxes, proper motions) and photometry for about 1.3 billion sources over the full sky. With these information, an HR-diagram for a huge numbers of stars can be built easily, which provides a very convenient tool to study stars at different evolutionary stages, including hot

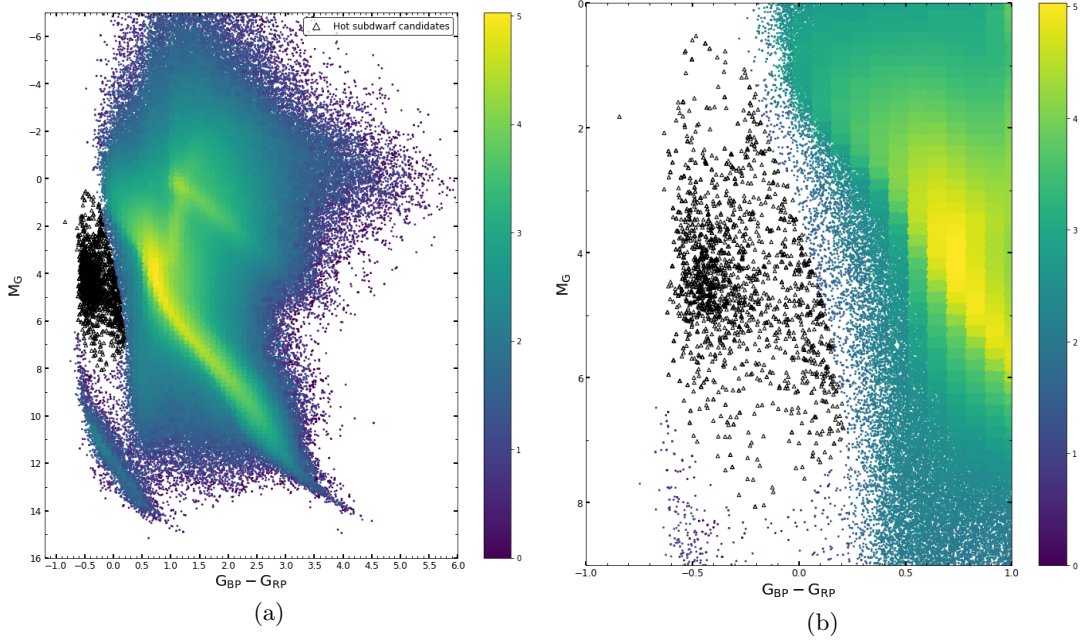


**Figure 1.** Panel (a): HR-diagram built with the objects filtered out by cross-matching Gaia DR2 database with LAMOST DR5 database (totally 8 852 848 objects), black triangles are the 2074 hot subdwarf candidates selected visually. The color bar represents the number of objects in each bin on a logarithmic scale. Panel (b): Magnified drawing for the region of hot subdwarf candidates.

subdwarf stars. LAMOST is a Chinese national scientific research facility operated by the National Astronomical Observatories, Chinese Academy of Sciences. It has a specially designed reflecting Schmidt telescope with 4000 fibers in a field of view of  $20 \text{ deg}^2$  in the sky (Cui et al. 2012; Zhao et al. 2006, 2012). LAMOST finished its pilot survey in 2012 and the first-five-years regular survey in 2017, respectively. The data from both the two surveys make up the fifth data release (DR5) of the LAMOST, in which spectra in the optical band (e.g., 3690–9100Å) for 8 171 443 stars, 153 090 galaxies, 51 133 quasars and 642 178 unknown objects have been obtained. This large spectral survey also provide us huge opportunities to analyze the spectra of many interesting objects, such as hot subdwarf stars.

Lei et al. (2018, hereafter Paper I) selected 734 hot subdwarf candidates from the HR-diagram built by Gaia Collaboration et al. (2018b). After analyzing the corresponding LAMOST spectra, they identified 294 hot subdwarf stars in their sample, which demonstrated an efficient and powerful method to search for hot subdwarf stars by combining the Gaia database and the LAMOST spectral database. However, to see the different structures clearly, the HR-diagram used to select hot subdwarf candidates in Paper I was built by the objects which are strictly filtered out from the database of Gaia DR2 (for the detailed filters see Gaia Collaboration et al. 2018b and Paper I ), without considering the completeness of the sample. Actually, only 65 921 112 (e.g., about 33%) stars were selected from the whole 1.7 billion Gaia DR2 sources to build the HR-diagram by Gaia Collaboration et al. (2018b) , and only 734 of the selected candidates have LAMOST spectra, in which 490 spectra have good quality for further spectral analysis. It means that many hot subdwarf candidates were not included in the HR-diagram used in Paper I due to the strict data selection. Therefore, to recover the maximum number of hot subdwarfs by combining the Gaia DR2 database with the LAMOST DR5 database, we built a new HR-diagram by using all the objects from cross-matching the whole Gaia DR2 database and the whole LAMOST DR5 database, without any filters. Then we selected the hot subdwarf candidates in the new HR-diagram. This method can conserve most of the hot subdwarf stars which were not included in Paper I. This paper is structured as follows. In Section 2, we described our new candidates selection process. Spectral analysis and classification is presented in Section 3. Our results are shown in Section 4. Finally, a discussion and a summary are given in Section 5 and 6, respectively.

## 2. TARGET SELECTION

We cross-matched the whole Gaia DR2 data with the LAMOST DR5 catalog, and found 8 852 848 common objects. The HR-diagram was built by using the Gaia  $G_{BP} - G_{RP}$  color and absolute magnitude of the Gaia  $G$  band (i.e.,  $M_G$ )

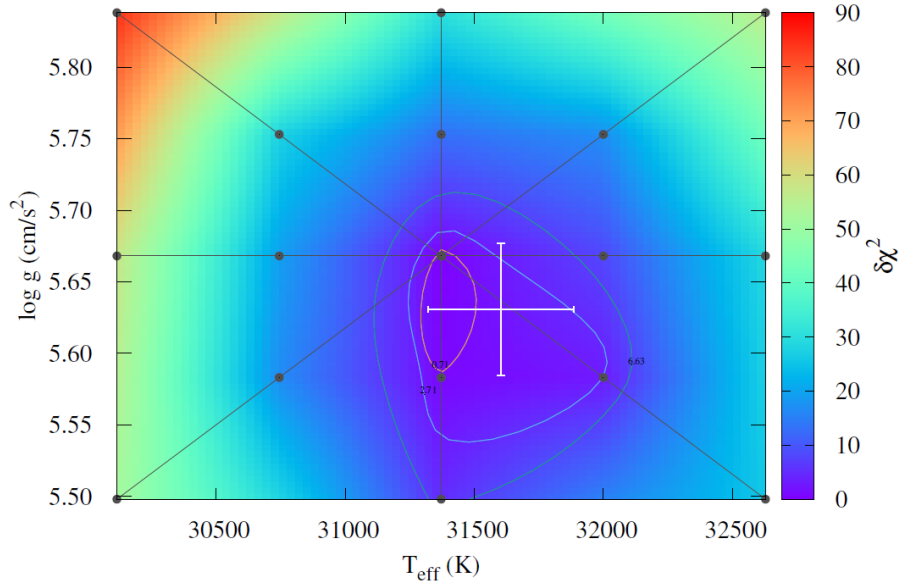


**Figure 2.**  $T_{\text{eff}}$ - $\log g$  correlation and two dimensional error determination for a sdB star (LAMOST obsid: 223907015). The color bar shows the chi-square variations with the parameters. The contours show the confidence intervals for 60, 90 and 99%. See the text for details.

for all the common objects, where their parallaxes are available and not negative.  $M_G$  is calculated by the following equation:

$$M_G = G - 5\log_{10}(1000/\varpi) + 5, \quad (1)$$

where  $\varpi$  is the parallax in milliarcseconds (mas) and  $G$  is the apparent magnitude in the Gaia  $G$  band. To include the maximum number of hot subdwarfs in our sample, we did not apply any filters when building the HR-diagram. Since the candidates selected from this step will be fitted by synthetic spectra, no extinctions are considered in our HR-diagram. These measures ensure that the new selection method obtains a larger sample of candidates than the one in Paper I.

Panel (a) in Fig 1 shows the new HR-diagram. Due to the influences of extinctions, the main-sequence (MS) appears much wider, and the red giant branch (RGB) can not be distinguished from the MS. Fortunately, the white dwarf (WD) sequence and hot subdwarf sequence separate more clearly from the MS in the HR-diagram due to their much bluer colors than the majority of MS stars. The black triangles in Panel (a) are the candidates we selected visually around the hot subdwarf regions. To include hot subdwarf stars as many as possible in our sample, we extended our selection region very close to the left of the wide MS. Because some real hot subdwarf stars could settle into these regions due to large extinctions, or some hot subdwarf binaries with low mass companions also would locate in these areas. The magnified area for the candidates selection is showed in Panel (b) of Fig 1 for clarity.

Using the method described above, we totally selected 2074 candidates in the HR-diagram. As we expected, this sample is about 3 times bigger than the one selected in Paper I (e.g., 734 candidates with LAMOST spectra in Paper I). After removing the objects we had analyzed in Paper I, we have 1431 objects left in our sample. We also removed the objects with the signal to noise ratio (SNR) in  $u$  band less than 10 to guarantee a good quality of spectral analysis in our follow up study, which reduced the sample to 592 objects. After removing double-lined spectroscopic binaries, and spectra with obvious spectral contamination from nearby cool stars (e.g., Mg I triplet lines at 5170 Å and/or Ca II triplet lines at 8650 Å), we finally selected 441 candidates suitable for a spectral analysis.

### 3. SPECTRAL ANALYSIS AND CLASSIFICATION

We employed the spectral analysis tool, XTGRID (Németh et al. 2012, 2014), to analyze the observed LAMOST spectra as we did in Paper I. This program fits the observed data with synthetic spectra (SYNSPEC version 49; Lanz et al 2007) calculated from non-LTE model atmospheres (TLUSTY version 204; Hubeny & Lanz 2017). The best fitting model is searched for iteratively with a successive approximation method along the steepest-gradient of the  $\chi^2$  field. The parameter uncertainties have been estimated by mapping the  $\Delta\chi^2$  field until the 60 per cent confidence level at

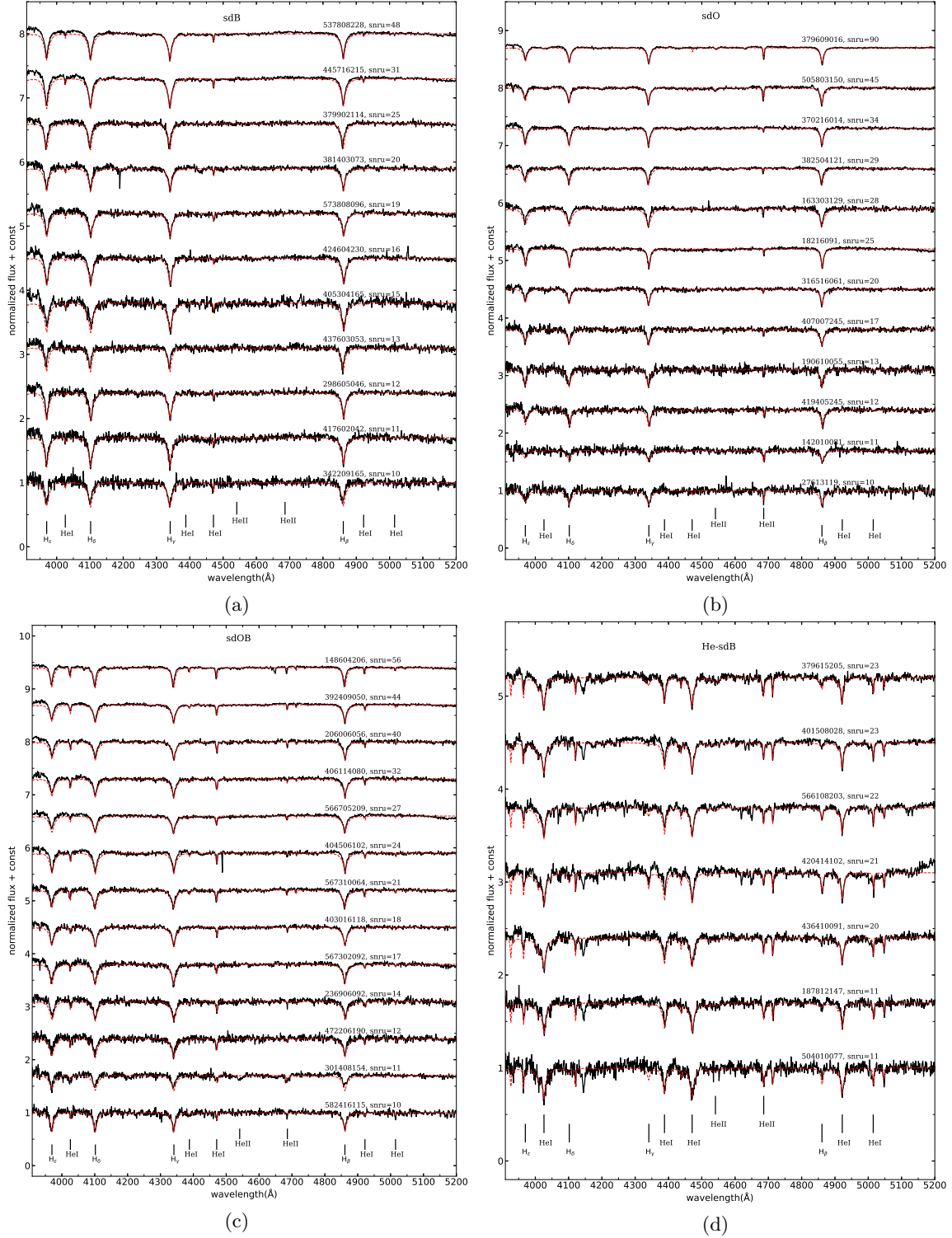


**Figure 3.** Some fit examples for different types of hot subdwarf stars in our sample. The SNR in  $u$  band decreases from top to bottom in each panel. The important H and He lines are marked at the bottom of each panel.

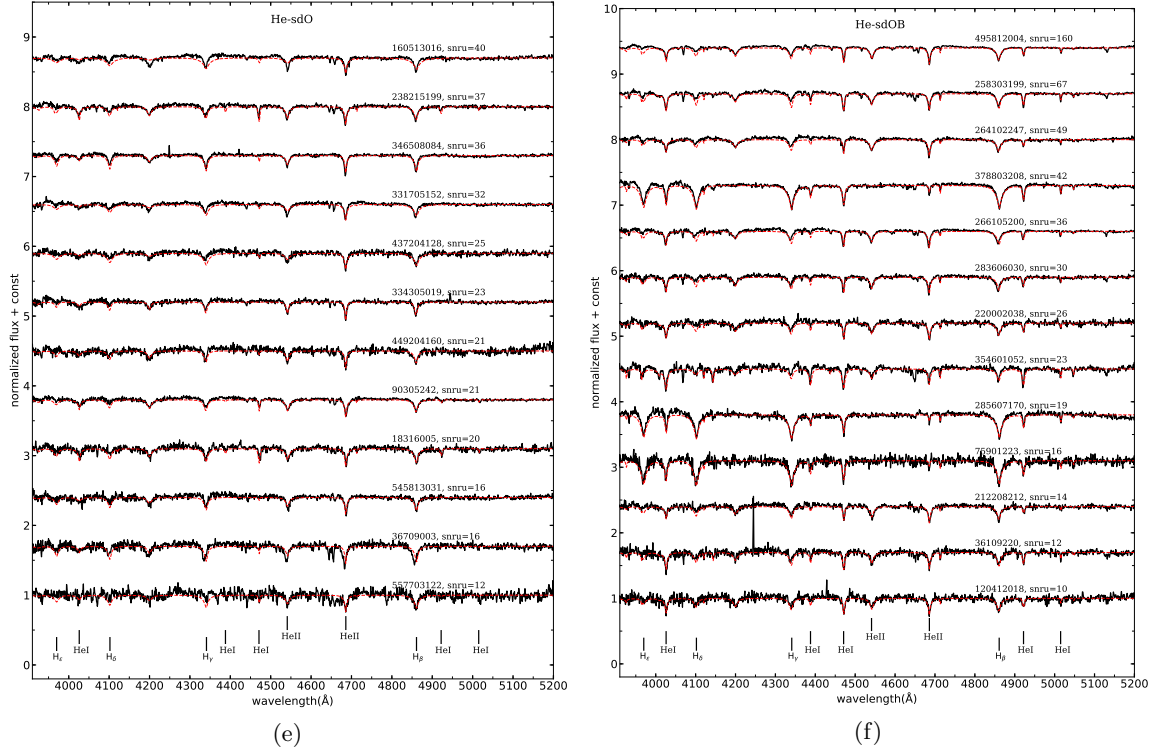


Figure 3. Continued.

the given number of free parameters was reached. Standard uncertainties in XTGRID are derived in one dimension, because parameter correlation calculations are extremely costly with non-LTE models and global, grid-less fitting. The global minimization procedure is pursued until all gradients vanish and parameter correlations are minimal. Then each parameter is changed until the 60 percent confidence level is reached to find the corresponding error bars. Our procedure applies the degree of freedom corresponding to the number of free parameters to set up confidence interval limits. Then a parabola is fitted to the data points obtained for a given parameter, and the error bar is measured from the parabolic fit.

We have upgraded XTGRID with a new procedure to calculate two dimensional errors and uncover the correlation between  $T_{\text{eff}}$ - $\log g$ . Fig 2 shows an example of the  $T_{\text{eff}}$ - $\log g$  correlation and error determination for a sdB star (LAMOST observation ID (obsid): 223907015). The color bar shows the chi-square variations with the parameters. XTGRID follows the chi-square gradients of all parameters to find the best fit for the observation. The final model is represented here by the intersection of the black lines. During error calculations new models are calculated radially outward from the best fit until the confidence limit is reached. The data points along the lines represent the values that have been calculated from model atmospheres. The missing grid points have been interpolated from their neighbors. The color coding is the interpolated and smoothed chi-square field around the best fit. The contours show the confidence intervals for 60, 90 and 99%. From these data asymmetric error bars are derived. Then, in an additional step, the asymmetric error bars are recalculated to symmetric errors, as represented by the white error bars.

Fig 3 gives some examples of the best fitting models for different subdwarf types. In each panel, the black solid curves represent the normalized LAMOST spectra, while the red dashed curves represent the best-fitting synthetic spectra. The long integers in the right of panel are the LAMOST obsids. From Panel (a) to (f), the best fitting models for sdB, sdO, sdOB, He-sdB, He-sdO and He-sdOB are presented respectively. In each panel, the SNR of  $u$  band decreases from top to bottom. By fitting the observed spectra, we obtained the atmospheric parameters for the 441 hot subdwarf candidates. As we did in Paper I, candidates with  $T_{\text{eff}} \geq 20\,000$  K and  $\log g \geq 5.0$  cm s $^{-2}$  are identified as our hot subdwarf stars, while candidates with  $\log g < 5.0$  cm s $^{-2}$  and  $\log g < 4.5$  cm s $^{-2}$  are considered as blue horizontal branch (BHB) stars and B type MS stars, respectively (Németh et al. 2012).

We adopted the same classification scheme as in Paper I to classify our hot subdwarfs (see Paper I, Moehler et al. 1990, Geier et al. 2017a). Stars with dominant H Balmer lines, but no or weak He lines are classified as sdB stars.

Stars with dominant H Balmer lines together with weak He I and He II lines are sdOB stars; Stars which present dominant H Balmer lines together with weak He II lines are sdO stars. Stars with dominant He II lines together with weak or no He I and H Balmer lines are He-sdO stars. Stars that show dominant He I lines, but weak He II and H Balmer lines are He-sdOB stars, while stars with dominant He I lines, but no He II and H Balmer lines are He-sdB stars<sup>1</sup>.

#### 4. RESULTS

By using the method described in Section 3, we identified 388 hot subdwarfs in this study. Based on the classification scheme of Paper I, 186 sdB, 73 He-sdOB, 65 sdOB, 45 sdO, 12 He-sdO and 7 He-sdB stars are classified, respectively. We also cross-matched our hot subdwarfs with the hot subdwarfs cataloged by Geier et al. (2017a), Németh et al. (2012), and Luo et al. (2016), and got 253, 12 and 50 common stars, respectively. Note that nearly all the hot subdwarfs in Németh et al. (2012) and Luo et al. (2016) are cataloged by Geier et al. (2017a). It means that 135 new hot subdwarf stars are found in this study, which have not been cataloged before. Furthermore, Among the 253 common stars with Geier et al. (2017a), only 91 stars have their parameters available in the catalog, which are mostly taken from Németh et al. (2012) and Luo et al. (2016).

The parameters of the 388 hot subdwarf stars are listed in Table 1. Columns 1-4 give the right ascension (RA), declination (DEC), LAMOST\_obsid and Gaia source\_id. Next, columns 5-7 give the  $T_{\text{eff}}$ ,  $\log g$  and  $\log(n\text{He}/n\text{H})$  fitted by XTGRID. Columns 8-10 list the SNR in the  $u$  band, the apparent magnitude in the Gaia  $G$  band and the spectral classification, respectively. The common stars in Geier et al. (2017a) are marked with \* in Table 1, and the common stars with Németh et al. (2012) are marked by †, while the common stars with Luo et al. (2016) are marked by ‡. In table 1, the symbol ' >' in  $\log(n\text{He}/n\text{H})$  denotes an upper limit of the He abundance, when XTGRID could not find the error bars mostly due to the low quality of the spectra.

##### 4.1. Parameter diagrams

Panel (a), (b) and (c) in Fig 4 show the  $T_{\text{eff}}\text{-}\log g$ ,  $T_{\text{eff}}\text{-}\log(n\text{He}/n\text{H})$  and  $\log g\text{-}\log(n\text{He}/n\text{H})$  diagram for the 388 identified hot subdwarfs, respectively. The He-sdB, He-sdO, He-sdOB, sdB, sdO and sdOB stars are marked by magenta stars, aqua left triangles, red diamonds, black circles, green squares and blue up triangles, respectively. The zero-age HB (ZAHB) and terminal-age (TAHB) with  $[\text{Fe}/\text{H}] = -1.48$  from Dorman et al. (1993) are represented by two dashed lines in Panel (a), while the He-MS from Paczyński (1971) is denoted by a black solid line. We also show three evolution tracks for hot HB stars by three brown dotted curves with masses from top to bottom: 0.495, 0.490 and 0.488, respectively. The dotted line in Panel (b) is the linear regression line used to fit the He-rich sequence by Edelmann et al. (2003), while the dot-dashed line is the regression line used to fit the He-weak sequence by Németh et al. (2012). The red horizontal dashed line in Panel (b) and (c) denotes the solar He abundance ( $\log(n\text{He}/n\text{H}) = -1$ ).

Panel (a) of Fig 4 shows that most of the sdB (i.e., black circles) and sdOB stars (i.e., blue up triangles) are well in the region defined by the ZAHB and TAHB lines, which indicates that these stars are He core burning stars. In addition, our sdOB stars present higher temperatures and gravity than sdB stars. On the other hand, most He-sdOB stars (red diamonds) evolve off the TAHB and cluster near  $T_{\text{eff}}=45\,000$  K and  $\log g=5.6\text{ cm s}^{-2}$ , but we also find a few He-sdOB stars in the bottom areas defined by the ZAHB and TAHB, and overlap with our sdOB stars. Both sdO stars (i.e., green squares) and He-sdO stars (i.e., aqua left triangles) show very high temperatures (e.g.,  $T_{\text{eff}} > 40\,000$  K), and some of them even have their temperatures over 70 000 K. Moreover, the gravity of these two groups also cover a wide range. 7 He-sdB stars are found in our sample, which are marked by magenta stars in Fig 4. These stars have the temperature around 40 000 K, but a wide coverage of gravity.

Two distinct He sequences (e.g., He-rich sequence fitted by the dotted line (Edelmann et al. 2003) and He-weak sequence fitted by the dot-dashed line (Németh et al. 2012)) are clearly presented in Panel (b). This obvious characteristics in field hot subdwarfs was first found by (Edelmann et al. 2003) and confirmed later by many other authors (Németh et al. 2012; Geier et al. 2013; Luo et al. 2016; Paper I). One can see from Panel (b), the He-rich sequence consists of sdB, sdOB, He-sdOB and He-sdB stars, while the He-weak sequence consists of all the sdO stars and several sdB stars with very low He abundances (e.g.,  $\log(n\text{He}/n\text{H}) < -3.0$ ). However, due to the low resolution of the LAMOST spectra (e.g.,  $\lambda/\Delta\lambda=1800$ ), the He abundances for some of He-poor sdB stars are difficult to obtain

<sup>1</sup> Actually, He-sdB stars could present a wide range of He abundance and temperature (Ahmad & Jeffery 2006; Naslim et al. 2010), e.g., a type of intermediate He-sdB (e.g., iHe-sdB,  $-1 < \log(n\text{He}/n\text{H}) < 1.0$ ) and a type of extremely He-sdB (e.g., eHe-sdB,  $\log(n\text{He}/n\text{H}) > 1.0$ ) are present in Naslim et al. (2010). However, the He-sdB stars in our sample represent the hot subdwarfs with the highest helium abundance (e.g.,  $\log(n\text{He}/n\text{H}) > 1.0$ ). Therefore, one can easily make it clear that the He-sdB stars in our study correspond to eHe-sdB stars in Naslim et al. (2010), while our He-sdOB stars correspond to iHe-sdB stars in Naslim et al. (2010).

**Table 1.** Information on the 388 hot subdwarf stars identified in this study. From left to right, it gives the right ascension (RA), declination (DEC), LAMOST\_observatory, and Gaia source\_id. Next the  $T_{\text{eff}}$ ,  $\log g$  and  $\log(n\text{He}/n\text{H})$  are listed from the XTGRID fits. Next, the SNR for the  $u$  band, the apparent magnitudes in the Gaia  $G$  band and spectral classification are listed, respectively.

RA <sup>a</sup> LAMOST	DEC <sup>b</sup> LAMOST	obsid <sup>c</sup> LAMOST	source_id Gaia	$T_{\text{eff}}$ (K)	$\log g$ (cm s <sup>-2</sup> )	$\log(n\text{He}/n\text{H})^d$	SNRU	$G$ Gaia(mag)	spclass
0.065682*	17.648047	472903166	2773760665114010880	36610±810	6.06±0.13	-1.85±0.09	37	16.55	sD OB
0.535283*	19.987016	385805170	2846319155418023424	31560±450	5.58±0.06	-3.00>	15	15.60	sD B
2.188996*	12.288674	66613068	2766032919436757504	32230±330	6.00±0.08	-2.26±0.13	15	14.62	sD B
2.923521	19.340418	364410161	2797293512483062912	27310±170	5.45±0.03	-2.84±0.08	49	14.74	sD B
3.593379*	28.615494	2915216	2859984160805522176	24180±80	5.44±0.04	-3.00>	45	12.65	sD B
4.681331*	1.023214	266708166	2547139876837313920	29090±150	5.47±0.05	-3.32±0.07	44	14.87	sD B
4.822343	40.502298	475310178	38038477929991424	26620±640	5.07±0.06	-2.71±0.26	15	16.34	sD B
5.353299	40.482537	90110033	380338531092183424	26580±520	5.34±0.04	-2.41±0.12	19	15.51	sD B
5.98014*	42.151544	90103101	382086995098288896	30320±220	5.55±0.06	-2.41±0.09	18	15.79	sD B
6.36564*	8.965084	248813198	2750667003920099200	29700±180	5.39±0.05	-2.79±0.23	16	15.60	sD B
6.439609	31.591527	284601234	2862287843823854848	26180±340	5.39±0.03	-2.27±0.05	38	15.52	sD B
6.528333	44.555064	382607056	382781542850500352	35770±330	5.75±0.07	-1.63±0.09	13	17.25	sD OB
6.949183*	34.674052	75901223 <sup>d</sup>	365939429892439320	33100±470	5.72±0.04	-0.76±0.04	16	15.77	He-sD OB
7.287603*	4.939857	182909073	2554910434747250944	33870±450	5.68±0.07	-3.29>	20	14.98	sD B
9.522662	43.74734	472206190	387661209812972928	36180±640	5.85±0.10	-1.46±0.15	12	16.15	sD OB
12.949002	27.003799	157506158	2808769596378258048	31780±330	5.82±0.14	-1.95±0.13	13	15.81	sD B
16.574205	41.576104	182701066	374540943716955392	26090±910	5.26±0.07	-2.18±0.12	24	15.96	sD B
18.225359	32.633936	386014113	313700498585403776	44940±550	5.73±0.10	0.82±0.09	15	16.05	He-sD OB
18.822416*	14.471761	385201146	2590919234398332544	42160±5940	5.49±0.10	-2.14>	13	15.32	sD O
18.976123*	26.233403 <sup>d</sup>	90305242	294818409307323904	55970±1350	5.68±0.10	0.58±0.13	21	14.42	He-sD O
19.738333*	-0.429333	20615234 <sup>d</sup>	2533806305483837440	29060±60	5.53±0.01	-3.15±0.15	16	14.82	sD B
20.095889*	39.849842	405010223	371711041304831616	28900±210	5.35±0.02	-2.84±0.09	34	15.41	sD B
20.91954*	30.04227	386001132	309391787394140288	29260±340	5.34±0.05	-1.97±0.09	11	16.50	sD B
21.126275*	6.816381	476409178	2566039072968204288	33890±350	5.66±0.04	-1.78±0.08	15	16.44	sD OB
21.587303	1.575993	354801221	2558457317524344704	49470±5840	5.92±0.14	-2.24±0.27	13	17.33	sD O
22.893792	32.623252	15209050	316170482737881728	73770±5630	5.34±0.13	-1.36±0.12	14	15.30	sD O
23.574204	26.388729	267314156	295620885292213248	28950±720	5.33±0.08	-2.44±0.54	14	16.28	sD B
26.036859	54.036332	468901095	408127652396870400	44900±520	5.79±0.42	-2.34±0.10	40	16.24	sD O
26.587053	45.69302	486404140	350797947892605952	29370±90	5.80±0.02	-2.83±0.10	28	17.45	sD B
29.296454*	20.654967	378509232	97013488627139328	34630±740	5.83±0.14	-1.54±0.07	21	15.39	sD OB
29.942499*	44.22208	191610229	346721341030064640	43970±1190	5.72±0.16	1.51±0.66	15	15.31	He-sD OB
31.084296	29.459688	293313054	30019923940638336	29590±60	5.65±0.02	-3.00>	13	16.20	sD B
31.265314	46.264437	306908165	352951036474046848	26900±100	5.25±0.03	-1.60±0.03	120	11.52	sD B
32.385219*	43.12014	83912135	35163354665907200	26570±360	5.42±0.05	-2.63±0.19	11	14.34	sD B
32.725888*	1.796436	290209126	2514184283536110720	42940±510	5.59±0.11	0.39±0.10	34	13.68	He-sD OB
33.959493	29.345947	405907157	108002248353357312	24270±90	5.63±0.01	-3.00>	46	14.01	sD B
34.935812*	24.790013	379615205	10280310454235008	39860±680	5.42±0.37	2.03±0.04	23	16.38	He-sD B
35.111382*	32.434422	386615187	10258330100450688	31040±320	5.67±0.07	-3.15>	22	16.76	sD B
35.358014	8.988819	266809027	23700286669971584	40690±20	5.53±0.42	1.53±0.05	20	17.00	He-sD OB
36.005261*	21.947266	379608221	99836961472298752	37010±370	5.86±0.06	-1.01±0.06	40	15.68	sD OB
36.301804*	23.806172 <sup>d</sup>	379609016	101826669497182720	52640±1380	5.46±0.08	-1.92±0.05	90	13.84	sD O
38.225357	37.072618	176806221	333636534183932416	35590±930	5.66±0.12	0.28±0.76	17	15.85	He-sD OB
40.018332*	3.928428	160513016	2503706418759709184	65870±1270	5.19±0.16	0.19±0.08	40	13.98	He-sD O
41.412008*	13.432122	298408084	31918414533148928	32120±130	5.34±0.01	-1.53±0.02	27	13.21	sD B
43.689377	9.275102	369315189	2094843650455160	29370±270	5.65±0.05	-3.00>	12	17.71	sD B
45.303592*	18.681715	387107175	3592850943041152	30240±150	5.43±0.03	-3.00>	38	15.42	sD B
45.548188*	37.185967	163303129	142086971376178688	44530±1700	5.63±0.11	-2.54±0.23	28	15.50	sD O
45.650063	28.271376	249704157	116691791828603136	37070±230	5.87±0.07	-1.59±0.05	38	16.27	sD OB
48.4049*	15.105965	406503078	3100977125186752	42110±180	5.63±0.02	1.32±0.05	52	15.62	He-sD OB
50.255387	18.955313	417602042	56252977678408192	27360±540	5.40±0.05	-2.52±0.16	11	16.36	sD B
50.388316	8.192122	414808170	11015044926034816	33610±510	5.69±0.07	-1.74±0.05	23	15.94	sD OB
50.411157*	5.644444	8315230 <sup>d</sup>	9132341717393792	31550±220	5.84±0.05	-2.06±0.03	28	14.99	sD B
55.122076	24.499152	474303164	683343083635794304	24940±420	5.66±0.07	-3.00>	11	16.55	sD B
55.654757	20.022511	249804028	63139734399542528	44340±780	5.96±0.08	0.64±0.06	16	16.21	He-sD OB
58.70092	35.255844	301309205	218951870771462144	77920±4860	7.06±0.16	-1.28±0.23	24	16.84	sD O
59.293668	28.828236	269903217	166876629257005696	33470±630	5.31±0.10	-2.73±0.26	13	17.43	sD B
61.095407	26.131827	170611197	162522700605966400	30350±180	5.75±0.06	-3.34±0.22	15	15.72	sD B
62.768174	34.310777	200512196	170774775937438233	26840±480	5.43±0.05	-3.04±0.08	19	16.38	sD B
62.954352*	15.383123	251121160	3311822554365339776	37490±520	5.59±0.04	-3.23±0.15	56	14.67	sD O
64.404255	30.127843	504604071	165712109004835712	31570±190	5.60±0.04	-2.09±0.06	21	17.06	sD B
66.426054	-6.159812	386702207	3199598460537019008	42260±580	5.45±0.08	1.64±0.30	20	16.69	He-sD OB
71.786429	21.890949	197202040	341273868650055296	30430±300	5.39±0.08	-2.70±0.15	16	17.69	sD B
72.615315	15.986111	402814084	3405118997094684032	37480±270	5.73±0.07	-0.90±0.08	16	16.64	He-sD OB
74.313203	43.055659	422313143	205078336132788352	27680±540	5.48±0.08	-2.87±0.27	14	16.03	sD B
75.717784	16.44665	266202113	339340896284662656	44970±1750	5.16±0.19	-3.03±0.37	28	15.61	sD O
81.110577	15.08733	498205197	339073900517699968	35140±470	5.45±0.06	-3.11±0.21	12	16.93	sD B
81.286539	17.953808	374416146	3400347392320018176	34810±540	5.68±0.09	-2.30±0.09	30	15.67	sD OB
81.961523	16.909214	374415024	3397199529183763072	45490±730	5.40±0.09	0.62±0.13	40	15.66	He-sD OB
82.391388	4.122033	506809203	323648827993523584	33980±2120	6.00±0.12	-0.93±0.11	12	16.53	He-sD OB

<sup>a</sup>Stars labeled with \* also appear in the hot subdwarf catalog of Geier et al. (2017a).

<sup>b</sup> Stars labeled with † also appear in Németh et al. (2012).

<sup>c</sup> Stars labeled with ‡ also appear in Luo et al. (2016).

<sup>d</sup> “>” denotes an upper limit of  $\log(n\text{He}/n\text{H})$  for the object.

**Table 1.** Continued.

RA <sup>a</sup> LAMOST	DEC <sup>b</sup> LAMOST	obsid <sup>c</sup> LAMOST	source_id Gaia	T <sub>eff</sub> (K)	log g (cm s <sup>-2</sup> )	log(nHe/nH) <sup>d</sup>	SNR <sub>U</sub>	G	spclass
								Gaia(mag)	
83.163266	43.638849	499503037	195587076882426880	30010±220	5.58±0.10	-2.74±0.18	12	16.36	sdB
83.348132	21.438994	198702152	3403657609512772096	48580±1160	5.51±0.06	-3.00>	16	16.90	sDO
85.570863	12.830711	506005080	3340527779312131584	31100±390	5.59±0.05	-2.81>	11	16.84	sdB
86.096935	38.297225	381414035	189831438452843008	28200±380	5.16±0.06	-2.84±0.24	11	16.06	sdB
86.672165	32.32837	174308109	3448218449263806080	33050±460	5.90±0.13	-2.05±0.11	10	17.15	sDOB
86.798328	17.15543	420414102	3396486324095591040	36050±1680	5.53±0.08	1.52±0.04	21	16.40	He-sdB
87.875844	38.478464	381403073	3457951566709510912	33180±530	5.80±0.08	-2.26±0.10	20	16.12	sdB
87.980862	13.398042	404506102	3346423532459289088	32240±200	5.68±0.05	-1.70±0.05	24	16.05	sDOB
90.000993	11.476859	401508028	3342199204486994048	38530±470	5.57±0.09	2.69±0.04	23	16.28	He-sdB
93.024484	47.523367	546803066	969542451362654976	47330±830	5.05±0.10	0.49±0.06	35	16.22	He-sDOB
93.355911*	34.34843†	177305180	3452237404778065152	34880±430	5.78±0.04	-1.39±0.04	50	13.67	sDOB
93.506639*	33.491003	187306026	3440046359151100032	52700±2130	5.30±0.15	-3.32±0.34	24	16.70	sDO
93.633112	-7.131204	211406205	3007619194841792640	29540±140	5.43±0.05	-3.33±0.14	74	13.94	sDB
93.792659*	35.854813	185915228	3452919960980353920	28610±280	5.68±0.04	-2.58±0.06	28	16.45	sDB
93.949651*	34.780417	220504128	3452646281368418304	22640±550	5.71±0.07	-3.00>	25	16.06	sDB
95.688418	51.846152	551803036	995383482875359744	32360±590	5.61±0.10	-1.94±0.09	24	16.48	sDOB
95.878258	33.022396	185907227	3439445854003662592	38500±1070	5.35±0.09	-3.00>	30	16.19	sDO
96.176952	28.496275	332303054	3433651805682659200	32930±710	5.87±0.09	-1.80±0.12	16	17.23	sDOB
96.799818	23.152877	301408154	3377315754750660992	39790±390	6.19±0.07	-1.72±0.09	11	15.94	sDOB
97.454305	22.414013	274411112	337646895899845312	28110±280	5.57±0.05	-2.65±0.17	14	15.43	sDB
97.865182	50.14843	551801179	968154867688361856	25350±720	5.34±0.07	-3.08±0.27	22	16.60	sDB
98.397232	23.148759	220002038	3382340316731002368	46790±440	5.61±0.06	0.75±0.09	26	15.51	He-sDOB
98.719332	37.186158	302804228	943173001432279040	45470±960	5.20±0.10	0.56±0.10	17	17.50	He-sDOB
99.208728	29.323616	332312170	3434651369127681664	39060±410	5.56±0.09	-0.11±0.08	14	17.14	He-sDOB
99.308942	42.381702	317915162	958032042088084992	34870±450	5.97±0.07	-1.34±0.07	11	17.25	sDOB
99.660973	42.948122	475702062	964071899977558784	29760±270	5.37±0.03	-2.86±0.17	20	16.17	sDB
100.62136*	37.070349	206006056	943819308110646144	34830±330	5.82±0.10	-1.56±0.05	40	15.09	sDOB
101.28447	21.304168	319005070	337815577335873664	27260±260	5.30±0.07	-2.52±0.24	15	16.16	sDB
101.79684	13.370346	387309021	3352595366104656384	35580±250	6.03±0.04	-1.26±0.07	12	17.39	sDOB
101.89525	13.836488	387309030	3352835983053282304	31770±220	6.06±0.04	-2.46±0.18	18	16.83	sDB
102.31712*	38.572141	296103019	944390774983674496	33450±140	5.72±0.03	-1.96±0.06	41	15.52	sDOB
102.6123	16.662794	282306209	335812278254938112	28870±350	5.65±0.05	-3.00>	13	16.32	sDB
102.83762	52.007091	546308112	993122779593859584	30300±420	5.82±0.09	-2.38±0.18	13	16.30	sDB
103.216529*	29.006594	15710159†	887620515740571264	32270±380	5.74±0.06	-1.91±0.10	26	14.79	sDB
103.23504	12.049997	387306122	3351464724552173952	46200±900	5.70±0.10	0.01±0.07	11	17.13	He-sDOB
103.80732	15.948556	422403108	3355060020193888480	29400±420	5.40±0.13	-3.29±0.40	12	16.45	sDB
104.47756	12.242259	392004058	3160786559070298880	50480±780	5.50±0.08	-1.77±0.15	44	15.69	sDO
105.11577	23.132122	298605046	3380129503787793920	29250±200	5.48±0.06	-2.60±0.10	12	17.05	sDB
105.2623	9.693231	507814235	3157919887443293952	23300±610	5.56±0.05	-3.35±0.30	11	17.05	sDB
105.34676*	53.493837†	545813031	981727582818800128	73480±4480	5.07±0.12	0.85±0.65	16	14.93	He-sDO
105.449625*	28.568161	21003121†	88439390088530144	26710±550	5.40±0.09	-1.92±0.11	18	14.90	sDB
105.52333	13.673537	422401101	3353521803431070464	31610±160	5.76±0.05	-1.81±0.07	12	17.12	sDB
105.56337*	12.29816	392009130	3160836861727862400	27110±410	5.41±0.04	-3.18±0.10	46	14.74	sDB
105.66879	11.794911	392008093	3160522848078571008	42690±520	5.62±0.07	0.76±0.08	28	15.79	He-sDOB
105.73661	17.391982	372812146	3361273433424723712	29210±170	5.58±0.03	-2.13±0.07	20	15.78	sDB
105.77822	19.537799	174905039	3364990572999194880	37730±760	5.40±0.08	-3.21±0.32	16	15.93	sDB
106.64127	9.090862	507803187	3154729899269006336	28260±240	5.37±0.02	-2.85±0.16	25	16.35	sDB
107.11835	44.426357	436410091	953141929764017408	38760±750	5.98±0.48	3.35±0.09	20	16.30	He-sDB
108.15275	13.195084	389404129	3161149775864814720	38280±900	5.97±0.07	-1.43±0.07	13	17.24	sDOB
108.22018	42.643905	316516061	949617548319629824	47000±1340	5.71±0.04	-3.42±0.48	20	16.15	sDO
108.27216	18.417765	267011180	33630700354244348800	27180±460	5.80±0.02	-3.00>	29	15.85	sDB
108.31042	17.582952	267015014	33607290677719609216	29520±460	5.60±0.03	-2.47±0.05	25	16.00	sDB
108.33188	38.127736	187812147	946428174325154856	39780±930	5.58±0.12	3.65±0.06	11	16.69	He-sDB
108.37492	19.895661	175006165	3363513924586196224	27480±110	5.33±0.15	-2.56±0.12	15	16.88	sDB
108.6558	26.786667	281105033	883333703358019584	24650±290	5.07±0.12	-1.92±0.31	19	15.83	sDB
109.71113	12.844212	389406022	3166142933042903424	26120±580	5.54±0.10	-2.42±0.14	11	17.23	sDB
109.73439	10.44399	446310014	315653539750882944	31080±380	5.47±0.09	0.41±0.07	35	15.79	He-sDOB
109.84141	5.16679	492414173	3140714527629703552	35180±260	5.79±0.12	-1.56±0.04	24	16.39	sDOB
110.995849	4.499076	492404174	3139698956841267456	29850±60	5.25±0.04	-2.71±0.09	38	15.40	sDB
111.42846	52.723794	448315232	986474685615378816	25000±170	5.50±0.02	-3.00>	56	15.31	sDB
112.103*	41.831571	320613193	948767385313600128	38230±320	5.71±0.06	-0.11±0.07	13	15.73	He-sDOB
112.74626	33.618403	320101130	89346761549784544	35750±290	5.80±0.38	-2.55>	20	17.19	sDB
112.816215	3.47858	492406014	3136412997623472512	24850±290	5.09±0.04	-2.44±0.12	13	16.57	sDB
112.88153*	20.756841	270109111	864917013671899648	50930±2040	5.50±0.09	-1.58±0.11	28	15.64	sDO
113.065169	6.203372	492412181	314152548617295836	28910±170	5.54±0.08	-3.08±0.50	21	15.93	sDB
113.08392*	27.069038	21602071	872322087046515840	36640±890	5.91±0.10	0.48±0.04	10	16.64	He-sDOB
113.69226	34.355805	75815079	893594510306886784	26400±480	5.25±0.04	-2.45±0.08	24	15.46	sDB
114.30941	25.098511	228001126	868529562204066688	26760±410	5.29±0.06	-2.34±0.12	11	15.52	sDB
114.63907	51.47903	448308129	982729822026188928	26880±400	5.45±0.04	-3.26±0.32	11	15.63	sDB
114.73744*	40.328337	331705152	923580185261224576	105770±970	5.24±0.03	0.36±0.04	32	16.45	He-sDO
115.01244	39.775833	334305019	923342347152856576	89120±12800	5.13±0.05	0.34±0.07	23	15.54	He-sDO
115.09819*	20.826954	176203116	673058556816796288	33560±140	5.76±0.02	-1.64±0.04	63	15.54	sDOB
115.10468*	15.8653	499603225	3165813590653493760	32430±660	6.21±0.12	-3.00>	11	17.07	sDB
115.6535	13.175169	407404024	3163997712841285504	28330±410	5.27±0.04	-2.72±0.17	14	17.55	sDB
116.13832	59.994095	448915044	1086079547054989184	28470±570	5.64±0.07	-2.59±0.18	11	17.02	sDB
116.5139	33.743557	273608236	88212536707882672	26480±240	5.22±0.03	-2.43±0.07	49	14.99	sDB
116.55484*	33.552105	120412018†	88208781188480896	46150±560	5.51±0.10	0.67±0.09	10	15.85	He-sDOB
117.04707*	43.877754	403501067	925982721247295488	27430±530	5.54±0.06	-1.75±0.08	13	16.99	sDB

**Table 1.** Continued.

RA <sup>a</sup> LAMOST	DEC <sup>b</sup> LAMOST	obsid <sup>c</sup> LAMOST	source_id Gaia	T <sub>eff</sub> (K)	log g (cm s <sup>-2</sup> )	log(nHe/nH) <sup>d</sup>	SNR_U	G	spclass
							Gaia(mag)		
117.04874*	13.730365	417207114	3164383748798177792	22940±930	5.36±0.16	-2.68±0.34	13	15.66	sdB
117.21696*	45.817713	405304165	92727948229851392	27690±520	5.74±0.07	-2.41±0.15	15	16.07	sdB
117.26186*	12.803115	407409236	3152255890729006848	37580±840	5.53±0.09	-3.26±0.37	18	16.68	sdB
118.1429*	16.268133†	414013194	66988874675710464	50420±710	5.67±0.10	0.62±0.13	13	14.46	He-sdOB
118.47597*	25.519389	173809084	873767017124252544	33540±740	5.86±0.04	-1.87±0.12	30	15.68	sdOB
119.29932*	13.752347	392702198	654222339006166656	36110±900	5.99±0.16	-1.54±0.17	18	15.93	sdOB
119.845827	16.767125	18216091	66730879819941776	38880±900	5.17±0.07	-2.70±0.16	25	14.42	sdO
119.93739*	37.250873	285607170	907291264093243520	33980±390	5.82±0.07	-0.91±0.04	19	16.30	He-sdOB
120.63138*	39.374639	279209235	921064055980216320	35770±230	5.47±0.05	-1.34±0.07	47	15.19	sdOB
120.86637*	34.361297	78615208	905650346067635968	39300±410	5.43±0.04	-3.09±0.20	26	15.06	sdO
121.61706*	32.516504	78608160†	90215492984483456	32930±240	5.65±0.07	-1.30±0.06	16	15.39	sdB
121.61938*	24.349293	103802062	680914734899282560	28190±260	5.50±0.03	-2.49±0.06	18	15.00	sdB
121.99274	27.409538	2001056	683766356962547840	38780±630	5.39±0.11	-3.06±0.23	55	14.11	sdO
122.14079*	18.039414	283606030	668963357040208512	45980±610	5.37±0.10	0.67±0.06	30	16.64	He-sdOB
122.34152*	16.144793	392712156	656428099850193664	37730±1080	5.54±0.12	-3.00>	23	15.74	sdB
123.02008*	13.867944	388802203‡	653631869983111552	27630±460	5.27±0.08	-2.74±0.17	15	17.29	sdB
123.42883*	27.842981	404612236	684061777696508544	27430±220	5.52±0.04	-2.52±0.09	19	16.32	sdB
123.88002*	24.872947	404606240	682305655764689408	35360±670	5.55±0.10	-3.00>	29	16.36	sdB
124.032567*	48.064086	198809068	931348922106072704	24740±610	5.50±0.04	-3.08±0.11	41	15.18	sdB
124.82385*	42.560752	318008007	915859960070594176	32880±180	6.10±0.04	-2.18±0.05	14	16.24	sdOB
125.60942*	39.68863	105910059‡	908526118730334592	31510±470	5.80±0.10	-2.28±0.11	11	16.95	sdB
125.917117	8.327003	334913110	599294211494840704	28110±240	5.75±0.04	-2.48±0.16	12	14.70	sdB
127.5257*	47.864096	302901126	930769616916994048	27030±980	5.57±0.09	-3.43±0.52	19	16.06	sdB
129.016533*	15.870972	43203186‡	657873717121550976	26790±490	5.56±0.05	-2.49±0.08	14	15.40	sdB
129.050164*	19.298929	431714232	662771594747150976	35310±470	5.49±0.07	-1.69±0.10	12	15.71	sdOB
129.824905	10.631478	420802086	601444306482580992	27030±280	5.52±0.03	-2.73±0.07	47	15.18	sdB
130.870297*	8.410645	503814238	597102541222525056	25720±430	5.64±0.05	-3.00>	19	16.45	sdB
131.499846*	-2.658236	302304166	3072185163322482816	32540±780	5.86±0.09	-2.37±0.05	21	15.72	sdB
131.82875*	23.0086	316011216	689367475352913280	60270±1140	5.41±0.06	-1.61±0.07	36	15.28	sdO
132.677077*	2.76284	449404224	577999175230073728	27540±150	5.33±0.03	-2.50±0.09	30	15.61	sdB
135.7186*	32.221134	205006060	712415021480712448	36030±1120	5.78±0.30	-1.89±0.77	14	18.16	sdOB
136.199038*	31.547997	28303115‡	711773838699959296	38250±420	5.62±0.06	-0.73±0.06	20	15.12	He-sdOB
136.272592*	5.550386	424616225	580372234855001460	41170±20	5.60±0.01	1.68±0.12	22	14.06	He-sdOB
136.783847*	-3.103886	495812004	5762960596350664832	48630±1150	5.47±0.05	0.75±0.07	160	11.88	He-sdOB
137.58958*	59.50939	209716167	1039246845702047360	73690±7550	6.97±0.32	-1.74±0.24	12	15.34	sdO
138.536147*	3.967868	424604230‡	57898616300965320	29420±370	5.52±0.07	-2.70±0.17	16	15.44	sdB
138.779524*	18.787857	554312158	635660764741010304	27270±480	5.05±0.05	-1.42±0.06	13	15.88	sdB
140.528329*	8.325203	223715183	58748452889551552	32160±450	6.01±0.12	-1.77±0.08	17	15.59	sdB
140.978208	36.393264	213108067	810691780249660800	34210±260	5.62±0.05	-1.70±0.13	19	15.66	sdOB
141.167117*	30.836992†	189207170	700362419831670016	40480±130	5.46±0.24	0.82±0.04	75	14.57	He-sdOB
141.196371*	23.321494	275512146	639171814606295424	26010±210	5.49±0.02	-2.29±0.10	11	15.78	sdB
141.660741*	32.753077	434508092	701197911230156672	31700±150	5.82±0.04	-2.89±0.24	34	14.88	sdB
142.694923*	48.273269	208410025	825628714431805056	45830±450	5.78±0.06	0.75±0.11	56	10.64	He-sdOB
143.191496*	8.271814	219713039	588040469465211904	31710±420	5.73±0.04	-1.84±0.08	10	16.47	sdB
143.800665*	31.166788	26030391‡	697707952845002880	33660±280	5.85±0.05	-1.73±0.04	29	15.63	sdOB
143.922229*	16.353044	32106171	619153556155078272	30320±40	5.47±0.02	-3.00>	26	14.72	sdB
144.249525*	38.122706	342411212	800799439774706560	26820±880	5.60±0.08	-2.40±0.11	11	15.43	sdB
144.3178*	18.419783	142410002‡	633011250955383168	35260±200	5.60±0.02	-2.76>	59	13.10	sdB
144.584797*	55.097246	124705056‡	1021648582279419648	32480±390	7.06±0.07	-1.85±0.71	50	12.03	He-sdOB
145.729342*	6.593786	341903193	3853346290335592320	26740±380	5.51±0.03	-2.82±0.10	38	13.68	sdB
145.81592*	16.932532	526902074	620566974075395840	28560±540	5.54±0.08	-2.23±0.07	18	16.17	sdB
145.977337*	27.783209	447314049	648029329761019776	30570±260	5.51±0.01	-3.00>	89	13.21	sdB
146.188903*	46.592334	301015204	821716652060662144	33620±400	5.21±0.06	-2.60±0.16	15	16.80	sdB
146.872334*	27.274173	388912003‡	647193232966817280	29550±320	5.57±0.06	-2.88>	14	16.63	sdB
147.23733*	33.697501	188204008	793720783914955392	51270±470	5.94±0.09	-0.00±0.05	27	17.69	He-sdOB
147.74187*	18.438487	142508056‡	627130616093753600	34560±250	5.89±0.08	-1.78±0.06	12	16.12	sdOB
148.383114*	11.750013	406114080	613219762482485632	34780±510	5.83±0.11	-1.49±0.10	32	15.10	sdOB
148.831108	51.616397	293910209	828120310859359104	49140±860	5.61±0.13	0.78±0.21	74	12.61	He-sdOB
149.202242*	14.378333	210808231	615674873163301248	45520±180	5.24±0.07	0.84±0.09	69	14.31	He-sdOB
149.444189*	4.913523	445716215	3849270435091240192	26390±140	5.49±0.01	-2.45±0.03	31	15.32	sdB
149.966705*	3.50916	445703068‡	3848520258923494656	33770±220	5.30±0.03	-2.60±0.14	44	15.41	sdOB
149.98337*	35.666425	9010097	795785941630955392	46650±1320	6.11±0.15	-0.36±0.14	25	15.33	He-sdOB
153.42551*	26.10556	134015249‡	739156243780100352	52050±2820	5.37±0.08	-1.73±0.28	10	16.67	sdO
153.7891*	0.550186	315411004	383190550061334912	32980±360	5.84±0.07	-2.06±0.08	21	14.86	sdOB
155.124196*	42.839426	346404022‡	805690720323579456	39670±690	5.25±0.07	-2.54±0.19	32	15.28	sdO
158.819075*	40.354013	142615080‡	780253140863277184	31660±110	5.92±0.04	-2.24±0.02	93	11.46	sdB
159.16221*	19.867303	106016182	3987249901607922944	33980±450	5.80±0.04	-1.78±0.06	20	15.59	sdOB
160.346854*	50.738881†	18316005‡	836644480912524288	50230±1360	5.70±0.09	0.22±0.07	20	14.95	He-sdOB
160.376837*	18.703028†	296504043	398613802047393068	34890±520	5.98±0.03	-1.68±0.03	61	13.00	sdOB
163.185161*	24.990381	403016118	729598330934052480	33540±490	5.81±0.14	-1.90±0.06	18	16.73	sdOB
163.553054*	29.286844	392414214	731743061507469568	35890±610	5.96±0.08	-0.63±0.09	18	17.08	He-sdOB
163.5772*	49.833258	148604206‡	832980633290384256	34250±1180	5.21±0.05	-1.53±0.04	56	13.34	sdOB
164.49736*	47.052083	504010077	831501240400109824	39310±1160	5.83±0.18	1.86±0.07	11	17.23	He-sdOB
165.233143*	10.928443†	290014160	3868418219635118080	32320±90	5.93±0.05	-1.92±0.05	37	14.21	sdOB
165.75989*	-1.060761	404011209	3803624106785054848	29360±390	5.48±0.07	-2.52±0.10	16	16.46	sdB
166.34654*	49.583249	503916138	832788184395879424	78590±2370	5.36±0.05	-0.97±0.14	51	14.26	sdO
166.7103*	29.592403	392409050	73269231532422528	35630±400	5.86±0.05	-1.48±0.04	44	15.73	sdOB
166.85657	47.353497	504003005	783541848870827264	25510±890	5.63±0.11	-3.00>	19	16.75	sdB
167.335037*	26.790214	190610055	3998182792399323904	4					

**Table 1.** Continued.

RA <sup>a</sup> LAMOST	DEC <sup>b</sup> LAMOST	obsid <sup>c</sup> LAMOST	source_id Gaia	T <sub>eff</sub> (K)	log g (cm s <sup>-2</sup> )	log(nHe/nH) <sup>d</sup>	SNRU	G Gaia(mag)	spclass
169.64492*	19.829744	297308031	3978207002584425216	28090±230	5.42±0.01	-2.60±0.06	45	13.17	sdB
169.770304*	29.864886	27611095 <sup>‡</sup>	4023163971460301952	31520±340	6.19±0.07	-2.33±0.17	19	14.30	sdB
170.234298*	9.611609	419405245	3914988790544222976	47810±6960	5.64±0.11	-2.54±0.23	12	16.45	sdO
170.57449*	37.448018	439213135	760930907631979904	39140±280	5.45±0.06	-2.76±0.25	20	15.93	sdO
171.654513*	11.999694	419412143 <sup>‡</sup>	3917380026471466112	29340±290	5.44±0.06	-3.11±0.18	16	15.71	sdB
172.122092*	29.251333	27613119 <sup>‡</sup>	4022181695259436416	46740±2870	6.20±0.22	-1.91±0.13	10	15.06	sdO
172.798333*	19.611231	393415146	397757553672822400	30440±230	5.74±0.05	-3.00>	28	15.57	sdB
173.173392*	-6.614569	407007245	3593223417120115712	49200±1400	5.73±0.07	-2.92±0.26	17	16.24	sdO
173.41895*	56.106739	42512139 <sup>‡</sup>	844818765479387392	32380±720	5.11±0.08	-2.81±0.15	11	15.21	sdB
174.359894*	14.170597	571607128	3918117008499710848	35700±820	5.83±0.09	-0.38±0.04	33	13.25	He-sdOB
174.47542*	58.256857	449009063	846070525377462528	33830±1110	5.88±0.05	-2.27±0.10	22	16.18	sdOB
174.925071*	46.730407	140606089 <sup>‡</sup>	78622077662239488	30760±170	5.55±0.05	-3.00>	25	15.57	sdB
176.238472*	-3.948095	499808226	360036549671173504	28010±340	5.31±0.06	-2.88±0.13	21	15.88	sdB
179.001258*	34.123619	399012110	4028265945931548544	38180±310	5.42±0.05	-2.54±0.09	58	14.83	sdOB
180.921546*	25.519844	19002085	4006102059258774272	35060±630	5.63±0.13	-1.53±0.10	13	15.13	sdOB
182.250307	47.915233	448510114	1546073572415417856	25900±450	5.29±0.06	-1.97±0.09	14	16.61	sdB
182.319787*	16.198908	343510162	3922570885986104064	29840±60	5.67±0.06	-2.41±0.03	84	13.65	sdB
182.400326*	-3.552102	203010225	3598151393876907904	36140±850	5.88±0.02	-1.56±0.04	48	13.34	sdOB
182.953929*	16.562911	404103003	392261019283095984	68520±2560	5.64±0.24	-1.89>	17	16.61	sdO
189.77099*	47.630772	319211089	1543006141129419648	29650±100	5.75±0.20	-2.33±0.12	11	15.56	sdB
190.026263*	11.538483	220712168	3928326210186248832	34620±340	5.28±0.08	-2.43±0.22	11	16.00	sdB
190.630828*	11.733614	437602078	3928420360164984320	47940±690	5.56±0.23	0.75±0.12	50	15.71	He-sdOB
190.70374*	13.609056	437603053	3929230528435328640	34320±510	5.05±0.08	-3.15±0.79	13	17.59	sdB
192.0795*	3.834201	437115236	3703904449460695040	74290±18350	5.85±0.09	-1.32±0.08	20	16.83	sdO
193.034742*	11.850803	223907015	3927916302803458304	31600±280	5.63±0.05	-2.41±0.10	20	15.25	sdB
193.12335*	-3.024892	105710231 <sup>‡</sup>	3682304199935092096	29880±160	5.72±0.03	-3.00>	15	15.65	sdB
193.32712*	30.108144	144516050 <sup>‡</sup>	1465043619891174016	33350±140	5.68±0.06	-2.05±0.08	16	15.84	sdB
193.534896*	1.723411	212208212	369064877163531251	50770±910	6.03±0.09	0.01±0.06	14	15.53	He-sdOB
194.114387*	27.708522	301803019 <sup>‡</sup>	1463697323542956672	26330±160	5.75±0.06	-3.00>	28	15.82	sdB
195.246685*	0.953267	327515053	3689564206493682816	39660±410	5.70±0.04	-0.49±0.06	18	16.47	He-sdOB
195.944218*	26.775245	301808222 <sup>‡</sup>	1460356814139885568	45940±230	6.93±0.01	-0.73±0.12	42	15.60	He-sdOB
196.202858*	28.124981	34503131 <sup>‡</sup>	1461140216174118016	34360±1240	5.97±0.08	-3.41±0.57	13	15.46	sdB
196.433237*	11.978208	214502083	3737057611255721472	31840±290	5.63±0.05	-2.32±0.15	18	16.04	sdB
196.564867*	48.838822	149710037 <sup>‡</sup>	1554816510916988544	32570±110	5.69±0.02	-1.76±0.02	52	13.73	sdOB
198.206285*	54.545775	403709179	1564081030251770752	28560±510	5.34±0.05	-2.61±0.17	14	15.84	sdB
199.822539*	20.954433	401811071	3940518836361346304	51410±980	5.50±0.05	0.82±0.12	49	15.15	He-sdOB
200.184944*	5.983701	36109220 <sup>‡</sup>	3717383603022961792	43660±610	5.70±0.10	0.70±0.16	12	14.74	He-sdOB
200.848058*	26.275522	582314065	1449056067988016128	33770±480	5.89±0.07	-1.71±0.06	26	16.19	sdOB
200.896934*	36.133203	139410221	147368767171803520	36900±480	5.47±0.04	-0.20±0.72	109	11.64	He-sdOB
200.988725*	26.250672	219310248	1449053353568686336	27330±780	5.21±0.09	-2.21±0.14	11	17.31	sdB
201.134907	32.072558	202506130	1469357759922416256	22580±590	5.06±0.06	-2.17±0.11	15	16.64	sdB
205.38117*	4.912973	142010081 <sup>‡</sup>	3714909426982422272	59430±4100	6.38±0.11	-1.59±0.19	11	16.23	sdO
206.636362*	28.289811	448603239	1451833434359977216	28040±360	5.33±0.02	-2.93±0.07	68	14.87	sdB
207.566067*	60.410686	36709003 <sup>‡</sup>	1661062937982961664	54020±1310	5.62±0.15	-0.43±0.07	16	16.32	He-sdO
207.971317*	-1.496278	41804169 <sup>‡</sup>	3658738470295900800	30420±720	5.70±0.06	-3.39±0.23	10	15.66	sdB
208.89461*	16.004774	341310209	1243253467230351360	37380±390	5.69±0.05	-1.38±0.06	33	15.92	sdOB
208.913404*	14.910708	341302147	1231024630186706944	29210±190	5.48±0.04	-2.39±0.06	27	16.00	sdB
209.602612*	6.860208 <sup>‡</sup>	339610163 <sup>‡</sup>	37206554747924952	28470±380	5.41±0.08	-2.90±0.08	65	14.32	sdB
210.821432*	28.658128	323001369	1452740084776034944	47360±490	5.57±0.05	0.58±0.09	76	14.85	He-sdOB
211.499225*	31.409769	537808228	14543234158795954368	30540±220	5.73±0.04	-2.33±0.07	48	13.48	sdB
213.598658*	29.684781	233014059	1260997037988611648	24980±300	5.68±0.04	-3.00>	11	16.66	sdB
213.772692*	27.459303	233002202	1260448626498096000	28630±230	5.47±0.03	-2.40±0.13	19	16.72	sdB
214.401671*	-4.574742	115709085 <sup>‡</sup>	3642680992030225536	36370±390	5.79±0.07	-1.48±0.05	24	13.71	sdOB
214.587163*	-3.381686	449706090	364592008861401216	29790±290	5.79±0.03	-3.00>	17	16.51	sdB
214.84398*	29.780611	23300129	1284970278417991680	34740±350	5.62±0.11	-1.52±0.06	20	17.40	sdOB
216.248249*	3.328705	236906092	3668499109893566464	35200±330	5.82±0.32	-1.49±0.13	14	16.48	sdOB
216.49655*	28.787578	233008016	1283953332341515520	34250±200	5.64±0.02	-1.78±0.05	15	16.74	sdB
217.365692*	19.359703	316813056	123936476948085496	50580±1460	5.55±0.16	0.29±0.06	39	14.08	He-sdOB
218.77645*	28.797477	566705209	1281101268798929152	36500±320	5.85±0.05	-1.77±0.05	27	16.10	sdOB
221.02439*	34.353706	574013227	1292915830478091008	46830±310	5.72±0.17	1.02±0.12	38	16.03	He-sdOB
221.784749*	7.397089	140208168 <sup>‡</sup>	1171708961765771392	49380±890	5.43±0.15	0.78±0.07	32	14.63	He-sdOB
223.344967*	39.496492	242506213	1296418427846820608	30110±470	5.81±0.11	-2.68±0.28	15	16.16	sdB
223.61111*	47.334557	344015107	1590388529573233536	30350±40	5.74±0.02	-2.50±0.09	28	16.11	sdB
224.0603*	16.961273	566108203	1188049561085487872	38920±950	5.76±0.29	2.07±0.13	22	17.28	He-sdB
224.39335*	3.79988	457101145	1155001746247388800	29520±630	5.68±0.06	-2.58±0.14	14	16.76	sdB
226.152825*	12.803728	442407239	1181028908759001472	46180±460	5.48±0.09	0.52±0.09	40	15.45	He-sdOB
229.805583*	26.289058	462202202	1270423258548105728	30470±190	5.46±0.09	-3.00>	15	15.86	sdB
231.759504*	42.068681	573415155	1390836579404946560	30860±150	5.73±0.05	-2.90±0.15	24	16.31	sdB
231.77099*	11.14553	565710140	1169270800131487360	36990±290	5.61±0.04	-0.45±0.04	26	17.24	He-sdOB
232.084522*	10.50891	567310064	1165848673269627520	35120±320	5.75±0.06	-1.36±0.04	21	15.95	sdOB
232.217458*	9.528992	567302092	1165536789924111616	32720±170	5.88±0.04	-1.87±0.06	17	16.45	sdOB
232.746779*	2.306311	557703122	4421020604704127360	88700±29720	5.21±0.39	1.79±0.20	12	16.43	He-sdO
233.071679*	45.772572	582416115	139489866848350848	34680±680	5.35±0.22	-1.88±0.14	10	16.54	sdOB
233.374829*	52.113533	53103086 <sup>‡</sup>	1595357428778377344	31890±270	6.04±0.06	-2.38±0.09	12	13.99	sdB
233.796725	23.788525	328505074	122093499609899552	27150±260	5.37±0.03	-2.87±0.10	18	15.58	sdB
235.556658*	4.143363	449204160	4424645557102354432	68620±4760	5.17±0.23	0.86±0.58	21	15.90	He-sdO
236.678871	0.757753	457502165	4422600328035803264	52670±1420	5.43±0.12	-2.80±0.30	19	15.11	sdO
237.67498*	29.756532	339709096	1320813464131916416	30770±60	5.53±0.05	-2.69±0.08	34	16.41	sdB
239.140379*</td									

**Table 1.** Continued.

RA <sup>a</sup> LAMOST	DEC <sup>b</sup> LAMOST	obsid <sup>c</sup> LAMOST	source_id Gaia	T <sub>eff</sub> (K)	log g (cm s <sup>-2</sup> )	log(nHe/nH) <sup>d</sup>	SNR_U	G	spclass
								Gaia(mag)	
239.178931*	50.26042	437204128	1403149533383468928	63150±2470	6.54±0.10	-0.41±0.20	25	16.13	He-sdO
239.374454*	48.839656	437201058	1399993557054575232	43920±610	6.01±0.13	0.63±0.09	13	16.52	He-sdOB
239.69352*	19.371987	558416059	1203338412004998016	61690±9680	5.67±0.11	-1.39±0.07	28	16.81	sdO
240.88683*	51.80773	458002156	1403885518979474688	35500±640	5.92±0.09	-0.61±0.23	12	17.75	He-sdOB
242.385059*	22.630508	461109174	1206447693448896128	44740±530	5.64±0.11	1.89±0.10	20	16.34	He-sdOB
242.88709*	29.01083	342203079	1316998296222144768	30080±750	5.41±0.15	-2.66±0.17	12	16.83	sdB
242.95559*	19.397395	558412106	1201659389029469184	33090±170	5.81±0.05	-1.93±0.03	17	15.89	sdOB
243.365233*	8.898758†	233106152	4452964853466754048	31400±140	5.92±0.04	-2.19±0.06	90	14.63	sdB
243.572692*	3.997775	568307134	4437211291383115392	46690±850	5.60±0.05	0.65±0.06	23	15.58	He-sdOB
243.696*	42.459869	241910003	1381954385173920640	35200±1410	5.83±0.08	-1.53±0.05	30	14.38	sdOB
244.13037*	-0.648126	451409063	4407283954965874816	36490±690	5.53±0.08	-1.68±0.11	11	16.82	sdOB
244.84043*	29.918343	342209165	1318236621192489216	33060±290	5.93±0.13	-2.12±0.14	10	16.87	sdB
245.874442*	24.761389	238215199	1302449042967968640	53080±740	5.68±0.08	0.21±0.06	37	15.70	He-sdO
246.60941*	33.554169	344109041	1325657289591907456	44640±590	5.34±0.09	1.20±0.45	11	18.25	He-sdOB
246.725946*	8.426436	236512210	4404350981196959104	41520±40	5.64±0.04	1.10±0.05	46	14.91	He-sdOB
248.05109*	17.888424	146615140†	446716978778235664	36470±1150	5.62±0.24	-2.75±0.57	11	15.99	sdB
248.647179*	26.350464	566608204	1304379201270414592	51420±1060	5.70±0.11	-2.31±0.11	20	16.97	sdO
251.538521*	40.290433	152701066†	1355775219474985856	29810±130	5.69±0.01	-1.93±0.05	40	14.10	sdB
253.7016*	15.882959	546709115	4557895027682278784	43060±360	5.59±0.10	0.75±0.08	38	15.53	He-sdOB
255.65702*	24.589606	143802076†	457246901942466304	27590±690	5.46±0.06	-2.38±0.12	10	15.93	sdB
255.98617*	34.251398	565812178	1337803736279119616	28360±180	5.34±0.03	-2.54±0.12	14	16.72	sdB
256.02866*	28.90447	346705170	1308731137012654464	32720±320	5.92±0.07	-1.69±0.07	15	17.04	sdOB
256.04676*	29.596299	346704165	1308836793208539264	30660±350	5.53±0.05	-2.63±0.14	23	17.16	sdB
256.313389*	35.471812	576815103	133848577087459072	43090±240	5.79±0.03	0.91±0.08	42	15.58	He-sdOB
256.39427*	24.890831	143802233†	457212562871774720	34410±620	5.80±0.07	-1.58±0.07	10	16.86	sdB
258.269431	24.838763	564407046	4571972212486265216	27400±390	5.44±0.02	-2.84±0.34	11	17.07	sdB
258.790469	24.739852	564407018	4573406491044824448	34770±750	5.19±0.08	-2.82±0.26	10	16.93	sdO
259.37476*	32.12192	573808096	1335353634003198848	32540±410	5.76±0.07	-2.28±0.16	19	17.23	sdB
261.050108*	28.591214	227215215	458511303803479936	36350±210	5.89±0.03	-1.67±0.03	77	13.34	sdOB
262.794308	53.086861	462011209	1417526777492843136	27550±530	5.17±0.06	-2.64±0.21	12	17.02	sdB
265.676651	44.503737	568416221	1350113181268869632	37500±480	5.56±0.15	-2.41±0.23	11	16.02	sdOB
272.615979*	41.90375	239111121	211350620037874848	27760±190	5.37±0.03	-2.86±0.06	27	16.15	sdB
279.219563	57.462023	346803047	2154234138295606272	28290±300	5.71±0.07	-3.00>	15	16.47	sdB
281.163262	43.374406	457204145	2116887915892603520	28740±1030	5.83±0.17	-1.89±0.17	37	16.30	sdB
294.50684*	46.82906	354601052	1218531679610988672	40680±20	5.17±0.15	1.59±0.07	23	15.98	He-sdOB
314.217996*	3.596911†	370216014	173143563351386752	40220±560	5.27±0.04	-3.25±0.27	34	14.46	sdO
315.813279	4.684183	370211146	173307190869606167	29660±320	5.69±0.06	-2.85±0.28	17	16.58	sdB
317.098329*	1.032085	370208205	2690647825256267264	25480±500	5.33±0.04	-2.50±0.06	26	15.99	sdB
318.667075	20.911639	372014148	1789867186124831616	29020±210	5.32±0.03	-3.00>	10	16.38	sdB
319.635091	23.571516	258303199	1792255325381143040	43100±240	5.43±0.04	0.77±0.12	67	14.67	He-sdOB
319.858333*	20.365419	469903131	179047050770502144	43130±340	5.58±0.17	0.93±0.10	45	15.99	He-sdOB
320.456296*	20.371406	372015115	1790305753825533312	39600±320	5.33±0.06	-2.94±0.17	28	15.37	sdO
321.270667*	-0.035192	254804129	2687886088269786112	36740±580	5.73±0.08	-1.43±0.07	22	17.02	sdOB
321.356173*	8.319926	372503172	174025956575806848	33230±260	5.53±0.18	-1.33±0.28	11	16.59	sdOB
321.9556*	0.490044	254804227	268797791350851584	58450±10450	6.36±0.10	-1.80±0.19	13	17.98	sdO
323.510983*	16.573053	158213246	1772138591918813056	37680±570	5.85±0.03	-3.04±0.17	34	14.44	sdO
323.858475*	-6.962075	56403085†	2667642399870553984	25510±480	5.21±0.02	-2.63±0.11	13	13.50	sdB
325.608836	9.218803	369411090	174135229640649888	43970±570	5.91±0.12	0.46±0.09	15	17.57	He-sdOB
326.420157	-1.468957	266105200	267469624799898194	47260±360	5.72±0.11	0.37±0.05	36	15.26	He-sdOB
328.835563	11.297908	371315006	2726863230013742336	35470±130	5.80±0.04	-1.44±0.02	42	15.35	sdOB
329.345461*	11.985671	371311070	2728427319664072704	36080±300	5.93±0.06	-2.09±0.15	18	16.47	sdOB
329.4386*	-2.025295	266107138	2679677791586720896	29290±100	5.51±0.04	-2.79±0.12	13	16.52	sdB
329.725771*	21.409014	169010006	178108015977815472	29350±310	5.30±0.10	-2.78>	11	16.26	sdB
329.98546	14.30136	378803208	1768547964899107584	34370±700	5.92±0.04	-0.73±0.04	42	16.20	He-sdOB
331.015786*	14.777294	378809160	1768493259900525312	42900±820	5.65±0.08	1.08±0.05	44	15.79	He-sdOB
331.115839	4.936688	353607003	2696218874579171744	27460±730	5.79±0.07	-2.73±0.17	12	16.84	sdB
331.481656*	5.959966	353606228	2720511213901083264	73690±4430	6.15±0.11	-1.80±0.28	11	18.12	sdO
331.818739*	3.705491	61309195†	2684009283284602880	32180±130	5.97±0.05	-1.93±0.12	12	14.21	sdB
332.002469*	2.562084	381708131†	2683585696429935488	27610±300	5.62±0.01	-3.00>	53	14.12	sdB
332.08127*	6.048748	353606189	272041033709020160	46210±250	5.35±0.07	1.09±0.08	13	16.73	He-sdOB
332.776303	51.642346	503412047	2004114070560436736	33090±780	5.40±0.08	-2.69±0.24	13	15.20	sdB
333.826383	16.617652	505803150	1775141422597602176	50800±1280	5.53±0.05	-1.76±0.07	45	16.87	sdO
333.962114	1.60178	382503103	2679494173144971136	29590±420	5.33±0.07	-2.53±0.16	14	16.69	sdB
334.029951	15.060714	505805092	2735467282163538944	34620±600	5.89±0.06	-1.46±0.06	17	16.98	sdOB
334.07485*	13.85585	470416164	273420064947455232	23150±260	5.05±0.05	-2.19±0.03	19	15.83	sdB
334.529784	4.819463	368707127	2707980797138700672	51910±1320	5.41±0.07	0.25±0.07	24	16.70	He-sdOB
335.344036*	5.416204	75501161†	2708400230759920768	35340±290	5.86±0.07	-0.76±0.04	25	15.28	He-sdOB
335.66121*	0.856942	382504121	2679230771390593024	50190±1050	5.55±0.08	-3.09±0.15	29	16.31	sdO
337.765186*	12.285902	157014157	273081326537396896	41950±850	5.40±0.05	-3.00>	25	15.69	sdO
338.731397	31.39054	1203114	1900710357773768448	47320±520	5.93±0.50	0.47±0.06	19	16.47	He-sdOB
339.806068*	13.636279	157011113	2731836527264665856	32200±400	5.66±0.03	-2.88>	65	14.93	sdB
339.981606*	-0.877811	362205243	2653065864983035392	42060±230	5.45±0.03	1.20±0.06	30	15.07	He-sdOB
340.0594*	2.10893	362211023	2654860474117747200	28280±210	5.38±0.05	-2.58±0.11	19	15.90	sdB
340.0884	12.09255	379902114	2729936846409609728	30670±290	5.42±0.07	-3.00>	25	16.76	sdB
341.7299*	15.5164	354509102	2732552133240294272	41210±40	5.51±0.04	1.75±0.07	29	15.72	He-sdOB
343.076508*	22.301397	353313201	2836713031563656704	47740±630	5.35±0.09	1.31±0.29	26	16.03	He-sdOB
343.67627	10.23328	380403222	271797309002215168	32480±810	5.38±0.03	-2.65±0.14	26	16.79	sdB
346.361835	19.298441	381310006	2831429843832458752	28060±160	5.17±0.06	-2.60±0.17	10	17.04	sdB
347.558118*	34.032284	264102247	19115725405202900						

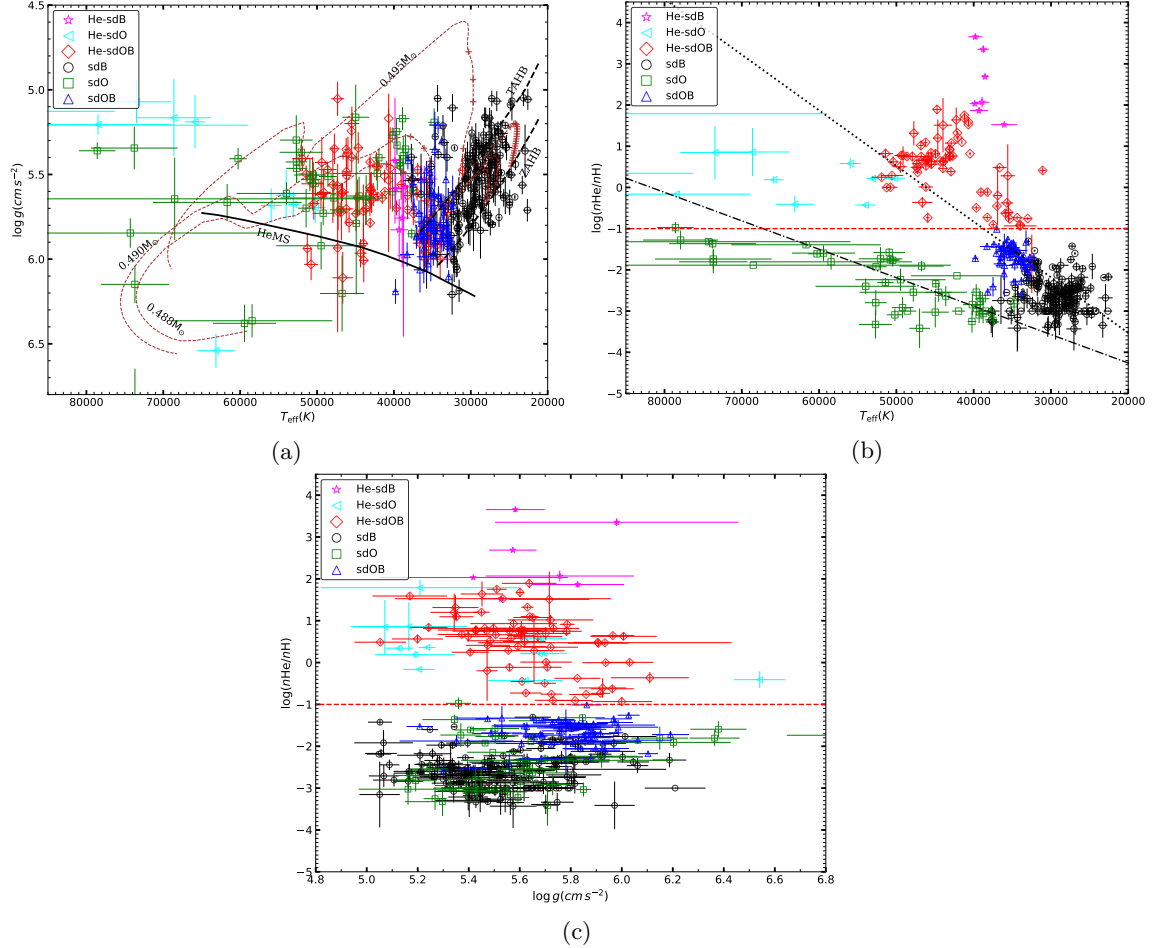


**Figure 4.** Panel (a):  $T_{\text{eff}}$ - $\log g$  diagram for the 388 hot subdwarf stars identified in this study. The ZAHB and TAHB sequences with  $[\text{Fe}/\text{H}] = -1.48$  from Dorman et al. (1993) are denoted by dashed lines. The He-MS from Paczyński (1971) is marked by black solid line. Three evolution tracks for hot HB stars from Dorman et al. (1993) are showed with brown dotted curves (see the text for details). Panel (b):  $T_{\text{eff}}$ - $\log(n\text{He}/n\text{H})$  diagram for the 388 hot subdwarf stars identified in this study. Different spectral classification types of stars are represented by different markers (see the text for details). The black dotted line and dot-dashed line are the linear regression lines fitted by by Edelmann et al. (2003) and Németh et al. (2012), respectively, while the red dashed line marks the solar value of He abundance. Panel (c):  $\log g$ - $\log(n\text{He}/n\text{H})$  diagram for the 388 hot subdwarf stars identified in this study.

or are obtained with very large uncertainties (e.g.,  $\log(n\text{He}/n\text{H}) < -3.5$ ). For such objects we report an upper limit of  $\log(n\text{He}/n\text{H}) = -3.0$  in this study. Considering this influence, one would expect that there could be more sdB stars make up the He-weak sequence in Panel (b). On the other hand, most He-sdO stars in our sample (i.e., aqua left triangles) are located in the region between the two regression lines, but much closer to the He-weak sequence. More interestingly, the He-sdOB stars in our sample (i.e., red diamonds) are split into two sub-groups by a distinct gap at  $T_{\text{eff}} = 40\,000$  K and  $\log(n\text{He}/n\text{H}) = 0.0$ . This distinct gap is also present in other studies (e.g., Fig 6 in Németh et al. 2012; Fig 8 in Luo et al. 2016; Fig 4 and Fig 5 in Heber 2016; Fig 7 in Paper I). Further work using higher resolution data and more complex models are needed for this feature, a detailed study on this aspect is out the scope of this paper. The distribution of hot subdwarf stars in our sample covers a wide range of gravity in Panel (c).

#### 4.2. Comparison with other studies

Like in Paper I, we also compared the atmospheric parameters of the stars that are common in our study and other studies, where the atmospheric parameters are available. Panel (a) and (b) in Fig 5 show the results from a comparison of our study and in Németh et al. (2012), Luo et al. (2016), respectively. One can see that the  $T_{\text{eff}}$  and  $\log(n\text{He}/n\text{H})$  in our study matched well with the values from the two other studies. However, a larger dispersion is present in

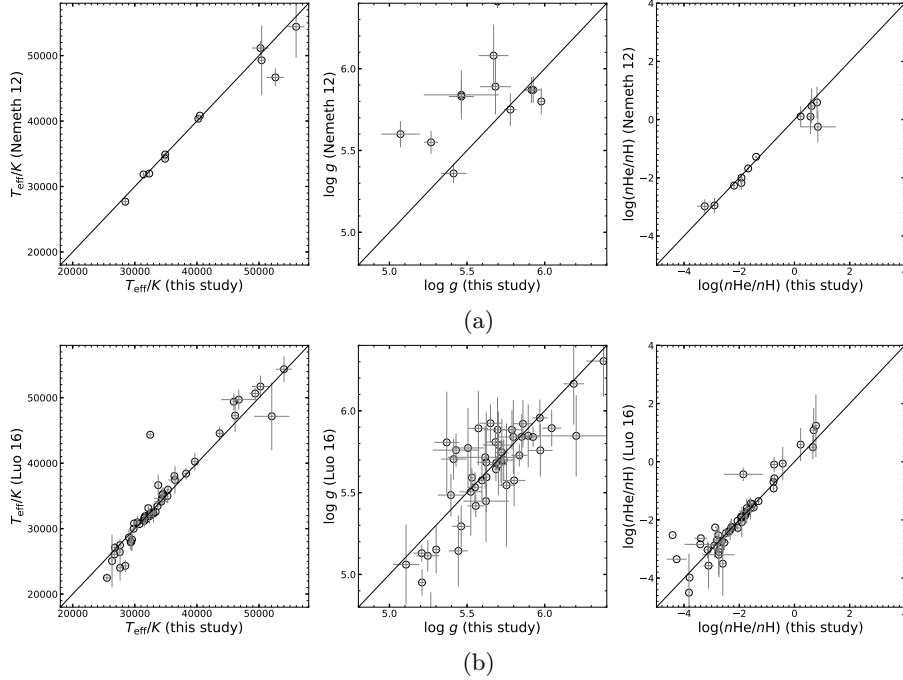


**Figure 5.** Panel (a): Parameter comparison with Németh et al. (2012). Panel (b): Parameter comparison with Luo et al. (2016).

gravity than in the other two parameters in Fig 5. Note that, the hot subdwarf spectra in Németh et al. (2012) are obtained in the *GALEX survey*, which have different quality (e.g., SNR) from our LAMOST spectra. Further more, the atmospheric models used in Németh et al. (2012) contain H, He, C, N and O compositions, while the atmospheric models used in this study contain H and He compositions only. On the other hand, although the atmospheric models and fitting procedure used in Luo et al. (2016) are the same with the ones we used in this study, but the spectra used for spectral analysis also could be different. Luo et al. (2016) selected candidates from LAMOST DR1, while we selected candidates from LAMOST DR5. The spectra could be different in SNR even for the same objects due to the repeat observations in LAMOST. These facts can result in the large gravity discrepancy between these two studies and our results. Nevertheless, the values of  $\log g$  in our study are comparable to the ones in other studies, and the comparison results showed in Fig 5 demonstrate the reliability of the spectral analysis in this study.

## 5. DISCUSSION

The counterparts of field hot subdwarf stars in GCs are the EHB and blue hook (BHk) stars (Heber 2009, 2016; D'cruz et al. 2000; Brown et al. 2001, 2016, Latour et al. 2014). Although these stars are burning He in the cores or even have evolved off the TAHB, the origin of the two counterparts could be different due to the very different environments, ages and initial compositions (for some formation scenarios of the two counterparts see Han et al. 2002, 2003; Chen et al. 2013; Zhang et al. 2012, 2017; Lei et al. 2015, 2016; Xiong et al. 2017; Wu et al. 2018).

Latour et al. (2018) analyzed the spectra of 152 EHB stars in  $\omega$  Cen, which were obtained with the FORS1 and VIMOS spectrographs equipped on the Very Large Telescope (VLT, ESO). The atmospheric parameters (e.g.,  $T_{\text{eff}}$ ,  $\log g$  and  $\log(n\text{He}/n\text{H})$ ) are derived by adopting non-LTE model atmospheres. Latour et al. (2018) found three distinct groups presented in their sample, e.g., H-sdB stars (the coolest H-rich stars), H-sdO stars (the hottest H-rich stars) and He-sdOB stars (see Fig 5 in their study). Moreover, the He-sdOB group can be further sub-divided into two sub-groups based on their He abundances. Since the sample size of the analyzed EHB stars in  $\omega$  Cen is big enough, Latour et al. (2018) also compared their results with four representative samples of field hot subdwarfs (i.e., Edelmann et al. 2003; Lisker et al. 2005; Stroeer et al. 2007; Németh et al. 2012). They found that the two distinct He sequences present in field hot subdwarfs also appear in  $\omega$  Cen EHB stars. However, the number fractions among different groups of EHB stars in  $\omega$  Cen are very different from the ones found in the field. The He-sdOB populations (corresponding to BHk stars) in  $\omega$  Cen are less represented in field hot subdwarf stars (e.g.,  $\approx 5\%$  in the galactic disk, and  $\approx 23\%$  in

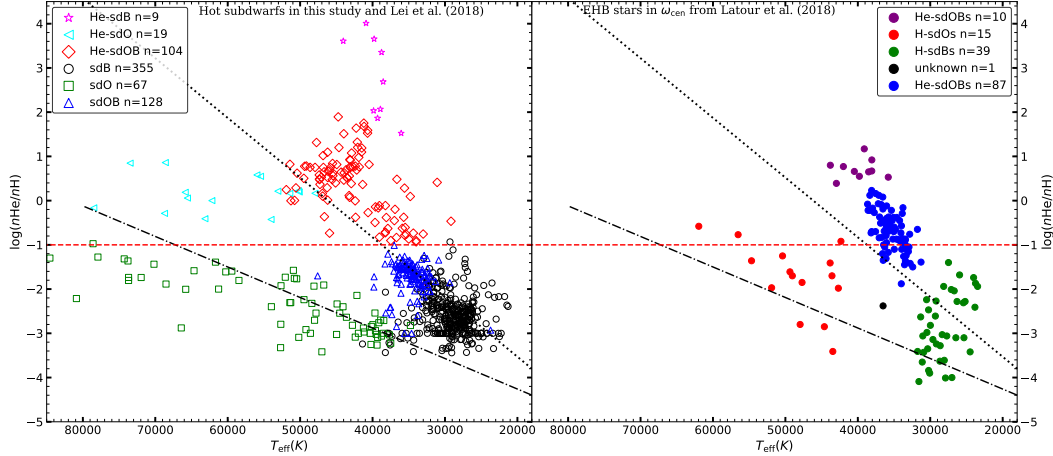


**Figure 6.** Comparing the 682 hot subdwarf stars identified in this study and Paper I with the  $\omega$  Cen EHB stars analyzed by Latour et al. (2018) in the  $T_{\text{eff}}\text{-log}(n\text{He}/n\text{H})$  diagram. The different markers and lines in the left panel have the same meanings as that of in Panel (b) of Fig 4. The solid circles with different colors in the right panel denote the different EHB groups found in Latour et al. (2018, see text for details). The error bars are not showed for clarity.

the galactic halo, while  $\approx 52\%$  in  $\omega$  Cen; Geier et al. 2017b). The results in Latour et al. (2018) demonstrated that BHk stars in GCs could experience a different formation origin from field hot subdwarf stars.

Similar results have been obtained by Heber (2016, see Fig 23 in their study) by comparing EHB stars in  $\omega$  Cen and NGC 2808 with the field hot subdwarf stars from the ESO-SPY project. They also concluded that He-rich hot subdwarf stars in the field are hotter than the He-rich EHB stars in GCs, and the He enrichment is higher in many field stars than that of the most He enriched stars in GCs.

To have a more clear understanding on this problem, we also compared the field hot subdwarf stars identified in this study and Paper I (682 stars in total, including 355 sdB, 128 sdOB, 104 He-sdOB, 67 sdO, 19 He-sdO and 9 He-sdB stars) with the EHB stars in  $\omega$  Cen analyzed by Latour et al. (2018). Fig 6 shows the comparison in the  $T_{\text{eff}}\text{-log}(n\text{He}/n\text{H})$  diagram between our field hot subdwarfs and the EHB stars in  $\omega$  Cen. The red dashed line marks the solar He abundance (i.e.,  $\log(n\text{He}/n\text{H}) = -1$ ). The dotted and dot-dashed lines are the same regression lines marked in Panel (b) of Fig 4, which are used to fit the He-rich sequence and He-weak sequence by Edelmann et al. (2003) and Németh et al. (2012), respectively. The 682 hot subdwarfs in our sample are denoted in the left panel by the same markers as in Fig 4, while the 152 EHB stars in  $\omega$  Cen are denoted in the right panel by solid circles with different colors.

As described by Latour et al. (2018), there are three distinct groups of EHB stars in  $\omega$  Cen<sup>2</sup>. The H-sdB stars in  $\omega$  Cen (i.e., green solid circles in the right panel) correspond to our sdB stars (i.e., black circles in the left panel). These stars have the lowest He abundance and temperatures (e.g.,  $\log(n\text{He}/n\text{H}) < -2$  and  $T_{\text{eff}} < 32\,000$  K) among the three groups. The He-sdOB group in  $\omega$  Cen can be sub-divided into two sub-groups, e.g., a high He abundance group (i.e., purple solid circles in the right panel) and a low He abundance group (i.e., blue solid circles). This group corresponds to our He-sdOB stars (i.e., red diamonds in the left panel). As we described in Section 4, our He-sdOB stars can be divided into two distinct groups based on their He abundances as well. Furthermore, the He-sdOB sub-group with low He in  $\omega$  Cen is much bigger in size than the He-sdOB sub-group with higher He (e.g., 87 vs 10, or the number fraction of 90% vs 10%). However, it is the opposite case in our He-sdOB samples, that the low He group is much smaller in size than the high He group (e.g. 33 vs 71, or the number fraction of 32% vs 68%) in our sample. Moreover, similar to the conclusion in Heber (2016), our He-sdOB stars in the high He group present higher temperatures (e.g., most of them have  $T_{\text{eff}} > 40\,000$  K) than the high He He-sdOB stars in  $\omega$  Cen (e.g, many of them have  $T_{\text{eff}} < 40\,000$  K). There is a distinct gap between H-sdB stars and He-sdOB stars in  $\omega$  Cen (see the right panel). As mentioned by Latour et al. (2018) this gap is predicted by the normal EHB models and delayed He-flash models (Miller Bertolami et al. 2008; Moehler et al. 2011, Lei et al. 2015, 2016). However, this distinct gap is not present in our sample (see the left panel), and it seems to be filled up by some sdB stars and sdOB stars in the same region. The H-sdO stars in  $\omega$  Cen

<sup>2</sup> One star in Latour et al. (2018) which can be added into any groups is marked with a black solid circle.

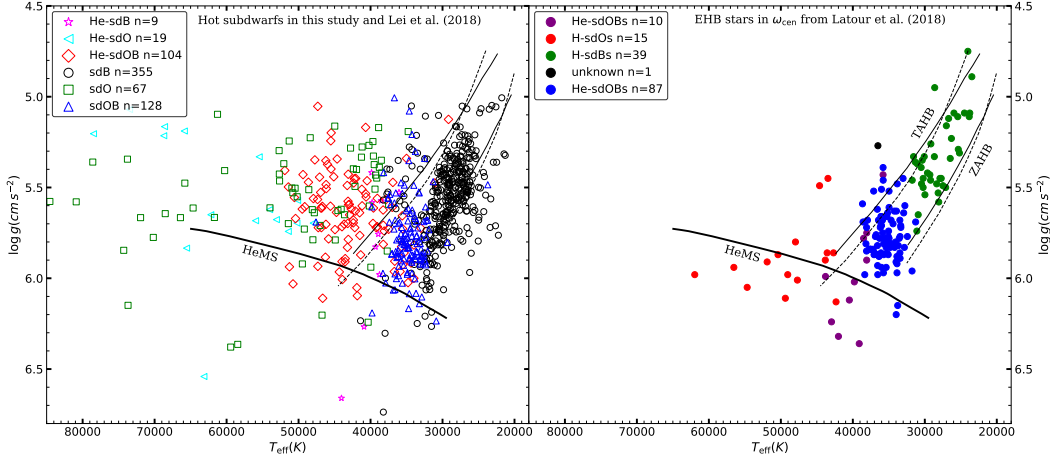


**Figure 7.** Comparing the 682 hot subdwarf stars identified in this study and Paper I with the  $\omega$  Cen EHB stars analyzed by Latour et al. (2018) in the  $T_{\text{eff}}$ - $\log g$  diagram. The different markers and lines in the left panel have the same meanings as that of in Panel (a) of Fig 4. The solid circles with different colors in the right panel denote the different EHB groups found in Latour et al. (2018, see text for details). The error bars are not showed for clarity.

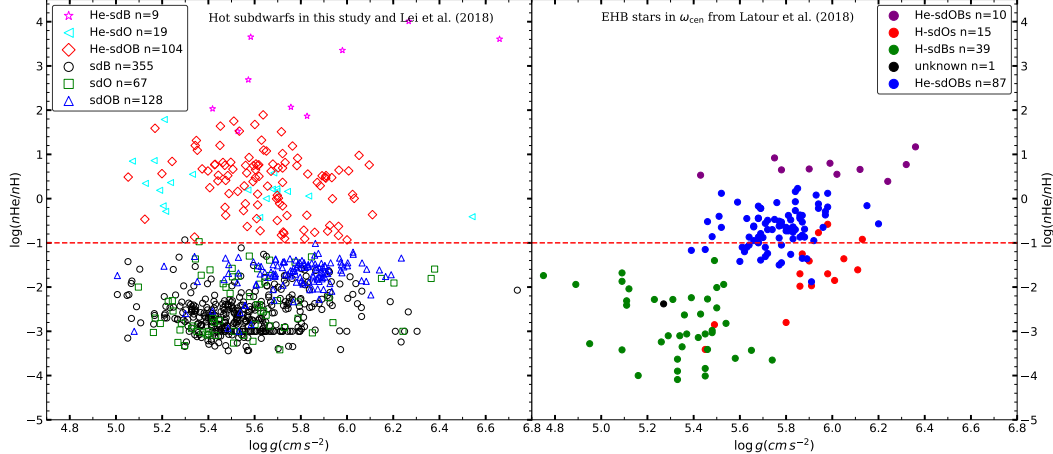
(i.e., red solid circles in the right panel) correspond to our sdO stars and He-sdO stars (e.g., green open squares and aqua left triangles in the left panel). Although the He-rich stars belong to this group of  $\omega$  Cen (e.g.,  $\log(n\text{He}/n\text{H}) > -1$ ) are much less in numbers than that of in our sample (e.g., 3 vs 19), but the number fraction are comparable for the two groups (e.g., 21% in our sdO and He-sdO samples vs 20% in  $\omega$  Cen H-sdO stars). In the left panel, we find 9 He-sdB stars (i.e., magenta stars), which have the highest He abundance (e.g.,  $\log(n\text{He}/n\text{H}) > 1$ ) in our sample, but this group is missing in  $\omega$  Cen.

Fig 7 shows the comparison of our hot subdwarfs and the  $\omega$  Cen EHB stars in  $T_{\text{eff}}$ - $\log g$  diagram. The two dashed lines are the ZAHB and TAHB sequences with  $Y = 0.24$  from Latour et al. (2018), while the two thin solid lines are the ZAHB and TAHB sequences with  $Y = 0.40$  from Latour et al. (2018). The thick solid line is the He-MS from Paczyński (1971). One can see that the gap between the H-sdB stars and He-sdOB stars in  $\omega$  Cen discussed above shows up clearly in the right panel of Fig 7. This gap is filled up by sdB stars and a few sdOB stars in our sample (see the left panel). The comparison between our hot subdwarfs and the  $\omega$  Cen EHB stars in the  $\log g$ - $\log(n\text{He}/n\text{H})$  diagram is showed in Fig 8. The panel on the right reveals a strong positive correlation between gravity and He abundance in  $\omega$  Cen. However, this correlation appears more obscure in the field (see the left panel).

The comparison results presented in this section come to a similar conclusion as in Latour et al. (2018) and Heber (2016) that the formation origins of field hot subdwarf stars and EHB stars in GCs are likely different in some aspects. Detailed theoretical models are needed to uncover the underlying differences of these populations. The two sub-groups of He-sdOB stars in the  $T_{\text{eff}}$ - $\log(n\text{He}/n\text{H})$  diagram which are clearly present in the EHB stars of  $\omega$  Cen also appear in our LAMOST field sample. However, this feature is not present in the ESO-SPY sample of field subdwarfs (see lower left hand panel of Fig 23 in Heber et al. 2016). This could be due to the fact that the size of the He-sdOB group in ESO-SPY sample is much smaller than that of our LAMOST sample.

## 6. SUMMARY

We have selected 2074 hot subdwarf candidates in the HR-diagram which was built by cross-matching the Gaia DR2 database with the LAMOST DR5 spectral database. After conducting a detailed spectral analysis, we identified 388 hot subdwarf stars among 441 candidates. The atmospheric parameters have been derived from non-LTE model atmospheres, and 186 sdB, 73 He-sdOB, 65 sdOB, 45 sdO, 12 He-sdO and 7 He-sdB stars were found in our study. Together with the 294 hot subdwarf stars found in Paper I, we totally identified 682 hot subdwarf stars by combining the Gaia database with the LAMOST database, among which, 241 hot subdwarf stars are newly identified that were not cataloged before. While 441 stars have records in the catalog of Geier et al. (2017a), but 255 of them have no atmospheric parameters. It means that we not only identified 241 new hot subdwarf stars, but also newly obtained atmospheric parameters for 255 hot subdwarf stars which were already cataloged in Geier et al. (2017a). These results indicate the efficiency of our method to select hot subdwarf candidates by cross-matching these two large survey



**Figure 8.** Comparing the 682 hot subdwarf stars identified in this study and Paper I with the  $\omega$  Cen EHB stars analyzed by Latour et al. (2018) in the  $\log g$ - $\log(n\text{He}/n\text{H})$  diagram. The different markers and lines in the left panel have the same meanings as that of in Panel (c) of Fig 4. The solid circles with different colors in the right panel denote the different EHB groups found by Latour et al. (2018, see text for details). The error bars are not showed for clarity.

databases. We expect that a large number of new hot subdwarfs will be discovered with the new data release of these surveys, which will make great contributions on the study of these special blue stars.

We confirmed the two distinct He sequences in the  $T_{\text{eff}}$ - $\log(n\text{He}/n\text{H})$  diagram. In addition, we found an obvious gap in our He-sdOB stars, which is also present in  $\omega$  Cen EHB stars. However, the number fraction of the members in the two sub-groups is very different between field samples and the  $\omega$  Cen EHB stars. Furthermore, the distinct gap between the H-sdB group and the He-sdOB group in  $\omega$  Cen EHB stars is not present in our sample. More interestingly, the He-sdB group which have the highest He abundance in our sample is completely missing in the  $\omega$  Cen. These results indicate a different origin of the field hot subdwarf stars and their GC counterparts.

We thank the anonymous referee for his/her valuable suggestions and comments which improve this work greatly. This work is supported by the National Natural Science Foundation of China Grant Nos 11503016 and 11390371, Natural Science Foundation of Hunan province Grant No.2017JJ3283, the Youth Fund project of Hunan Provincial Education Department Grant No.15B214, the Astronomical Big Data Joint Research Center, co-founded by the National Astronomical Observatories, Chinese Academy of Sciences and the Alibaba Cloud. This research has used the services of [www.Astroserver.org](http://www.Astroserver.org) under reference XD8O2C. P.N. acknowledges support from the Grant Agency of the Czech Republic (GAČR 18-20083S). This project was developed in part at the 2018 Gaia-LAMOST Sprint workshop, supported by the NSFC under grants 11333003 and 11390372. The LAMOST Fellowship is supported by Special Funding for Advanced Users, budgeted and administered by the Center for Astronomical Mega-Science, Chinese Academy of Sciences (CAMS). Guoshoujing Telescope (the Large Sky Area Multi-Object Fiber Spectroscopic Telescope LAMOST) is a National Major Scientific Project built by the Chinese Academy of Sciences. Funding for the project has been provided by the National Development and Reform Commission. LAMOST is operated and managed by the National Astronomical Observatories, Chinese Academy of Sciences.

## REFERENCES

- Ahmad, A., & Jeffery, C. S. 2006, Baltic Astron, 15, 139  
 Baran, A. S., Reed, M. D., Stello, D., et al. 2012, MNRAS, 424, 2686  
 Battich, Tiara., Bertolami, Marcelo M. Miller., Córscico, Alejandro H., et al. 2018, A&A, 614, 136  
 Brown, Thomas M., Sweigart, Allen V., Lanz, Thierry., et al. 2001, ApJ, 562, 368  
 Brown, T. M., Cassisi, S., D'Antona, F., et al. 2016, ApJ, 822, 44  
 Byrne, Conor M., Jeffery, C. Simon., Tout, Christopher A., et al. 2012, MNRAS, 475, 4728  
 Charpinet, S., Van Grootel, V., Fontaine, G., et al. 2011, A&A, 530, 3

- Chen, Xuefei., Han, Zhanwen., Deca, Jan., et al. 2013, MNRAS, 434, 186
- Cui, Xiang-Qun., Zhao, Yong-Heng., Chu, Yao-Quan., et al. 2012, RAA, 12, 1197
- D'Cruz, Noella L., O'Connell, Robert W., Rood, Robert T., et al. 2000, ApJ, 530, 352
- Dorman, Ben., Rood, Robert T., & O'Connell, Robert W. 1993, ApJ, 419, 596
- Drilling, J. S., Jeffery, C. S., Heber, U., et al. 2013, A&A, 551, 31
- Edelmann, H., Heber, U., Hagen, H.-J., et al. 2003, A&A, 400, 939
- Gaia Collaboration, Brown, A., Vallenari, A., et al. 2018a, A&A, 616, 1
- Gaia Collaboration, Babusiaux, C., van Leeuwen, F., et al. et al. 2018b, A&A, 616, 10
- Geier, S., Heber, U., Edelmann, H., et al. 2013, A&A, 557, 122
- Geier, S., Frst, F., Ziegerer, E., et al. 2015, Science, 347, 1126
- Geier, S., Østensen, R. H., Nemeth, P., et al. 2017a, A&A, 600, 50
- Geier, S., Østensen, R. H., Nemeth, P., et al. 2017b, Open Astronomy, 26, 164
- Geier, S., Raddi, R., Gentile Fusillo, N. P., et al. 2019, A&A, 621, 38
- Han, Z., Podsiadlowski, Ph., Maxted, P. F. L., et al. 2002, MNRAS, 336, 449
- Han, Z., Podsiadlowski, Ph., Maxted, P. F. L., et al. 2003, MNRAS, 341, 669
- Heber, U., Reid, I. N., & Werner, K. 1999, A&A, 348, L25
- Heber, U., Reid, I. N., & Werner, K. 2000, A&A, 363, 198
- Heber, U. 2009, ARA&A, 47, 211
- Heber, U. 2016, PASP, 128, 2001
- Hu, Haili., Nelemans, G., Aerts, C., et al. 2009, A&A, 508, 869
- Hu, Haili., Glebbeek, E., Thoul, A. A., et al. 2010, A&A, 511, 87
- Hu, Haili., Tout, C. A., Glebbeek, E., et al. 2011, MNRAS, 418, 195
- Hubeny, I., & Lanz, T. 1995, ApJ, 439, 875
- Hubeny, I., & Lanz, T. 2017, arXiv:1706.01859
- Jeffery, C. S., Baran, A. S., Behara, N. T., et al. 2017, MNRAS, 465, 3101
- Kawaler, S. D., Reed, M. D., Østensen, R. H., et al. 2010, MNRAS, 409, 1509
- Kawka, A., Vennes, S., O'Toole, S., et al. 2015, MNRAS, 450, 3514
- Kepler, S. O., Pelisoli, I., Koester, D., et al. 2015, MNRAS, 446, 4078
- Kepler, S. O., Pelisoli, I., Koester, D., et al. 2016, MNRAS, 455, 3413
- Kupfer, T., Geier, S., Heber, U., et al. 2015, A&A, 576, 44
- Lanz, Thierry., & Hubeny, Ivan. 1995, ApJ, 439, 905
- Lanz, Thierry., & Hubeny, Ivan. 2007, ApJS, 169, 83
- Latour, M., Fontaine, G., Chayer, P., et al. 2013, ApJ, 773, 84
- Latour, M., Randall, S. K., Fontaine, G., et al. 2014, ApJ, 795, 106
- Latour, M., Fontaine, G., Green, E. M., et al. 2015, A&A, 579, 39
- Latour, M., Heber, U., Irrgang, A., et al. 2016, A&A, 585, 115
- Latour, Marilyn., Randall, Suzanna K., Calamida, Annalisa., et al. 2018, A&A, 618, 15
- Lei, Zhenxin., Chen, Xuemei., Zhang, Fenghui., et al. 2015, MNRAS, 449, 2741
- Lei, Zhenxin., Zhao, Gang., Zeng, Aihua., et al. 2016, MNRAS, 463, 3449
- Lei, Zhenxin., Zhao, Jingkun., Németh, Péter., et al. 2018, ApJ, 868, 70
- Lisker, T., Heber, U., Napiwotzki, R., et al. 2005, A&A, 430, 223
- Luo, Yang-Ping., Németh, P., Liu, Chao., et al. 2016, ApJ, 818, 202
- Miller Bertolami, M. M., Althaus, L. G., Unglaub, K., et al. 2008, A&A, 419, 253
- Moehler, S., Richtler, T., de Boer, K. S., et al. 1990, A&AS, 86, 53
- Moehler, S., Dreizler, S., Lanz, T., et al. 2011, A&A, 526, 136
- Moehler, S., Dreizler, S., LeBlanc, F., et al. 2014, A&A, 565, 100
- Moni Bidin, C., Villanova, S., Piotto, G., et al. 2012, A&A, 547, 109
- Morrissey, P., Conrow, T., Barlow, T. A., et al. 2007, ApJS, 173, 682
- Naslim, N., Jeffery, C. S., Ahmad, A., et al. 2010, MNRAS, 409, 582
- Naslim, N., Jeffery, C. S., Hibbert, A., et al. 2013, MNRAS, 434, 1920
- Napiwotzki, R., Christlieb, N., Drechsel, H., et al. 2001, AN, 322, 411
- Németh, P., stensen, R., Tremblay, P., et al. 2014, ASPC, 481, 95
- Németh, P., Kawka, A., & Vennes, S. 2012, MNRAS, 427, 2180
- Németh, P. 2017, Open Astronomy, 26, 280
- Østensen, R. H., Silvotti, R., Charpinet, S., et al. 2010, MNRAS, 409, 1740

- Paczyński, B. 1971, *Acta Astron.*, 21, 1
- Rauch, T., & Deetjen, J. L. 2003, in *ASP Conf. Ser.* 288, Stellar Atmosphere Modeling, ed. I. Hubeny, D. Mihalas, & K. Werner (San Francisco, CA:ASP), 103
- Stroeer, A., Heber, U., Lisker, T., et al. 2007, *A&A*, 462, 269
- Vennes, S., Kawka, A & Németh, P. 2011, *MNRAS*, 410, 2095
- Vos, Joris., Vučković, Maja., Chen, Xuefei., et al. 2019, *MNRAS*, 482, 4592
- Werner, K., & Dreizler, S. 1999, *JCoAM*, 109, 65
- Werner, K., Deetjen, J. L., Dreizler, S., et al. 2003, in *ASP Conf. Ser.* 288, Stellar Atmosphere Modeling, ed. I. Hubeny, D. Mihalas, & K. Werner (San Francisco, CA:ASP), 31
- Wu, You., Chen, Xuefei., Li, Zhenwei., et al. 2018, *A&A*, 618, 14
- Xiong, H., Chen, X., Podsiadlowski, Ph., et al. 2017, *A&A*, 599, 54
- Zhang, Xianfei., & Jeffery, C. S. 2012, *MNRAS*, 419, 452
- Zhang, Xianfei., Hall, Philip D., Jeffery, C. Simon., et al. 2017, *ApJ*, 835, 242
- Zhao, Gang., Chen, Yu-Qin., Shi, Jian-Rong., et al. 2006, *ChJAA*, 6, 265
- Zhao, Gang., Zhao, Yong-Heng., Chu, Yao-Quan., et al. 2012, *RAA*, 12, 723
- Zong, Weikai., Charpinet, Stéphane., Fu, Jian-Ning., et al. 2018, *ApJ*, 835, 98